Bubble dynamics and bubble-induced agitation in the homogeneous bubble-swarm past a circular cylinder at small to moderate void fractions

Jubeom Lee[1] and Hyungmin Park[1,2,*]

[1]*Department of Mechanical Engineering, Seoul National University, Seoul 08826, Korea*

[2]*Institute of Advanced Machines and Design, Seoul National University, Seoul 08826, Korea*

(Received 29 December 2019; accepted 21 April 2020; published 18 May 2020)

Our study involved an experimental investigation of a homogeneous bubble-swarm past a circular cylinder, of which the size is more than five times larger than that of a bubble, while varying the upstream volume void fraction, $\langle\bar{\alpha}\rangle$, in a small-to-moderate range and cylinder diameter, D. The Reynolds number of rising bubbles is approximately 10^3. We focused on the way in which the preferred concentration of bubbles past a cylinder is established and how its wake is induced. We measured the gas- and liquid-phase velocity fields simultaneously by using a high-speed two-phase particle image velocimetry technique. Depending on the void distribution in the wake region, two regimes are classified. In the first regime (smaller $\langle\bar{\alpha}\rangle$), the bubbles tend to accumulate downstream of the side of the cylinder (along the shear-layer region), which is attributed to the mitigated lateral migration of bubbles *via* the balance between the drag force with the pressure gradient and shear-induced lift forces acting on them. As $\langle\bar{\alpha}\rangle$ increases, in the second regime, the shear-induced lift force becomes sufficiently strong to move the bubbles toward the center of the cylinder, resulting in the void fraction exhibiting a broad peak at this position. Based on the void distribution, the liquid flow forms an interesting wake structure behind the cylinder. For example, a wake-defect-like streamwise velocity profile and skew-symmetric Reynolds stress distribution are induced; however, the distortion by the circular cylinder is restored quite fast (within $5D$ along the streamwise direction). Increasing the cylinder size, however, delays the recovery of uniform flow statistics and reduces the turbulence level in the wake. Finally, we propose a model for bubble-induced fluctuation (Reynolds stress) that includes the contributions of the gradients of liquid velocity, void distribution, and bubble velocity. The model, which is an extension of the well-known eddy-diffusivity model, considers the effects of bubble-induced flow and multiple bubbles (void fraction). The bubble-induced Reynolds stress estimated by the present model is in a reasonably good agreement with the data measured downstream of the circular cylinder.

DOI: 10.1103/PhysRevFluids.5.054304

I. INTRODUCTION

In multiphase flows, the agitation caused by a dispersed phase results in substantial changes in the continuous phase flow statistics, such as turbulence modulation, as well as mass, momentum, and heat transport [1,2]. A bubble-swarm induced flow, where the gravity-driven bubbles are the only force driving the liquid flow that is otherwise at rest, is therefore a good configuration to characterize the relations between bubble dynamics (e.g., the void (α) distribution and bubble rise velocity) and the liquid-phase flow (mean and fluctuating velocities) [2–13]. For example, it was suggested that the rise velocity of gravity-driven bubbles decreases as the volume void fraction ($\langle\bar{\alpha}\rangle$) increases, for $0.005 \leqslant \langle\bar{\alpha}\rangle \leqslant 0.1$ at the bubble Reynolds number of $\mathrm{Re} \sim \boldsymbol{O}(10^2)$ [4,8,14]. Here, the

*hminpark@snu.ac.kr

upper bar and $\langle\ \rangle$ denote averaging in time and space, respectively. This phenomenon was further developed into the scaling relation of the mean bubble rise velocity to $\langle\bar{\alpha}\rangle^{-0.1}$ for small-to-moderate volume void fractions ($\langle\bar{\alpha}\rangle \lesssim 0.1$) [8]. This decreasing trend is attributed to the interference effect the downward liquid flux would have to develop between rising bubbles to balance the upward liquid flux that is entrained in the bubble wakes [2,8], although a more rigorous theoretical model to explain this phenomenon universally is still required. The bubble velocity fluctuation is more or less independent from $\langle\bar{\alpha}\rangle$, because of the path instability of the bubbles in the Reynolds number range under consideration.

The time-averaged and fluctuating nature of bubble-induced liquid flow is also of great interest [2–8,11,13–17]. A homogeneous bubble swarm induces liquid velocity of the order of the magnitude of the bubble velocity, in the vicinity of an individual bubble ($\sim 2.5d_b$ behind the bubble, where d_b is the bubble size) [5]; however, more enhanced models than the drift flux model need to be developed. Thus, in general, the bubble-induced liquid flow is locally accelerated where a larger population of bubbles exists; however, the flow is decelerated when this population declines [18,19]. However, the fluctuating liquid velocity has received more attention because its properties are comparable with those of typical single-phase flow turbulence. Because of the similarities between them, thus the agitation of the liquid flow is sometimes called bubble-induced turbulence (or pseudoturbulence) [3]. The collective influence of the wakes of individual bubbles has been considered to be the main cause of bubble-induced turbulence [9] and previous efforts have made it possible to understand some important characteristics of bubble-induced agitation (see Ref. [2] for a recent review). First, the bubble-induced liquid velocity fluctuations are scaled as $\langle\bar{\alpha}\rangle^{0.4}$ [2,5,7,8,13,14,19]. Owing to more enhanced liquid-flow entrainment in the bubble wake along the streamwise direction, the ratio of liquid velocity fluctuations in the streamwise and transverse directions is approximately 2 : 1. The probability density function (PDF) of liquid-velocity fluctuation as a result of rising bubbles [$\mathrm{Re} \simeq \boldsymbol{O}(10^2 - 10^3)$], however, has been used to investigate its turbulent nature. For example, the anisotropic characteristics of bubble-induced turbulence in the streamwise direction appears as a positive skewness in the streamwise velocity PDF [2,5,8,13], but the symmetric PDF profile is obtained for the transverse velocity owing to the axisymmetric (in a time-averaged sense) velocity distribution in the bubble wake.

As briefly introduced above, studies on bubble-swarm flows have substantially elevated our physical understanding of the interaction between rising bubbles and induced liquid flow. In practical situations, however, many circumstances exist in which the rising bubbles encounter solid obstacles [20,21]. In these situations, the external two-phase flow would be expected to involve more complex interactions among the gas-liquid-solid phases. Especially, a bubbly cross flow around a bluff body, which is a simple but fundamental representation of the problem, has not been fully investigated [20–26]. Because the behavior of bubbles in the vicinity of a bluff body is closely related to static pressure loss (i.e., drag variation), this mechanism has been the main topic of interest. In this regard, investigations established that the local void peaks appear near the liquid flow separation points and the center of the wake, the magnitude of which increases substantially as the inlet gas flux increases. However, bubble-induced agitation locally enhances momentum transport between the bulk liquid flow and the boundary layers on the body surface, delaying flow separation, and consequently resulting in the reduction of the total pressure loss [20,23,24]. However, in general, a descriptive explanation for this flow has been provided thus far; i.e., a detailed mechanism on the way in which the existence of a bluff body disturbs the temporal and spatial changes of the gas- (e.g., bubble size, velocity and distribution) and liquid-phase (mean and fluctuating velocities) statistics in the bubble-swarm flow has not yet been published. Another interesting issue would be to determine the way the bluff body wake is formed as a result of the bubble-swarm flow.

Therefore, in the present study, we experimentally investigated a homogeneous bubble-swarm past a circular cylinder in a water tank, focusing on the bubble dynamics and bubble-induced liquid fluctuation. Because the only source of liquid motion is the gravity-driven rising bubbles, this configuration would be useful to study the pure bubble effects on the liquid-phase flow. We used a high-speed two-phase particle image velocimetry technique, which has been successfully used for

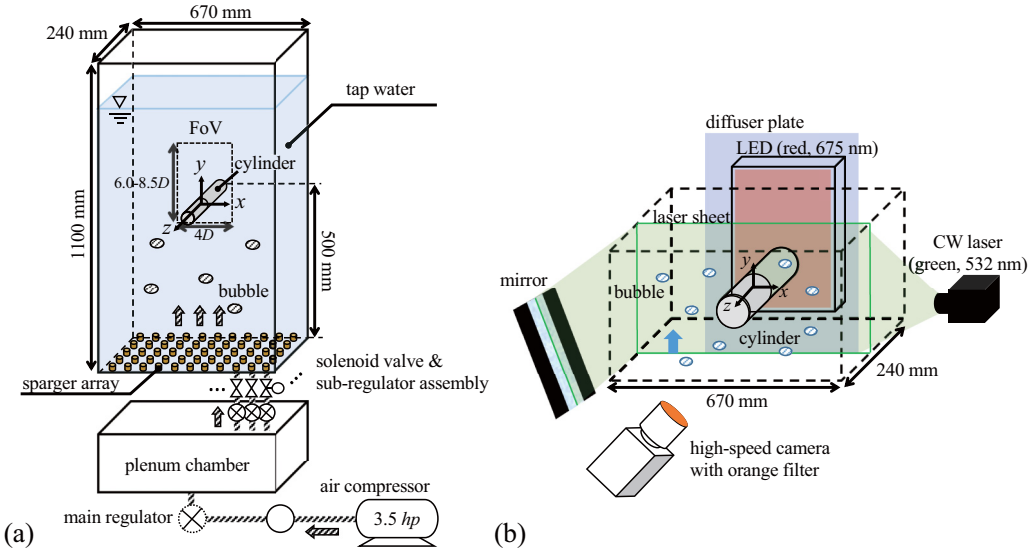

FIG. 1. Schematic diagram of experimental setup: (a) bubbly flow over a circular cylinder in a stagnant water tank; (b) two-phase high-speed particle image velocimetry measurement.

measuring the gas and liquid phases simultaneously [19,27,28]. We vary the volume void fraction in a small-to-moderate range as $\langle\bar{\alpha}\rangle = 0.3$–$2.1\%$, in which the Reynolds number of the bubbles is $\mathrm{Re} \simeq 1180$, indicating that its shape would be oblate ellipsoidal and a path instability occurs due to the asymmetric vortical structure in the wake [29–32]. To identify the effect of relative bubble size, we consider cylinders with two different sizes (D) as $\langle\bar{d}_b\rangle/D = 0.13$ and 0.2. Our study mainly focuses on (i) simultaneous measurement (visualization) of bubble behavior and bubble-induced liquid flow around a circular cylinder, (ii) physical interpretation of preferential concentration of bubbles in the cylinder wake, and (iii) characterization of the two-phase bluff-body wake flow. We are also interested in assessing the nature of bubble-induced liquid fluctuation, and we propose and validate a bubble-induced liquid fluctuation model, which is an improvement of that developed in a previous study of Kim *et al.* [19].

The paper is organized as follows. In Sec. II, we explain the experimental setup, and introduce the key parameters of our problem. An analysis of the bubble dynamics and details of the trend in void distribution are presented in Sec. III. Subsequent changes in the liquid-phase flow statistics, including the time-averaged and fluctuating velocities are discussed in relation to the bubble dynamics in Sec. IV. In Sec. V, a theoretical model to estimate the bubble-induced liquid fluctuation is proposed and compared with the experimental data. Finally, our results are summarized in Sec. VI.

II. EXPERIMENTAL SETUP AND PROCEDURES

A. Bubble-swarm flow past a circular cylinder

The experimental setup includes an acrylic water tank ($670 \times 240 \times 1100$ mm^3) with a circular cylinder installed, and a bubble generation system (a plenum chamber and sparger array) [Fig. 1(a)]. The tank is filled with tap water (at room temperature) to a level 950 mm from the bottom, and the circular cylinder (diameter $D = 20$ mm or 30 mm, length $L = 240$ mm) is located 500 mm from the bottom wall where the bubbles are generated. The location of the circular cylinder was chosen such that the bubble-swarm flow develops sufficiently for the bubble distribution (and bubble-induced

TABLE I. Characteristics of the considered gas-phase. Here, the subscript "∞" denotes a variable measured at the upstream location.

$\langle\bar{\alpha}\rangle$	$\langle\bar{d}_{b\infty}\rangle$ [mm]	$\langle\bar{v}_{b\infty}\rangle$ [mm/s]	$\langle\bar{\beta}_{\infty}\rangle$	Re	We	Eo	Mo
0.003	3.7	334	1.9	1240	5.8	1.89	1.11×10^{-11}
0.006	3.5	318	1.9	1120	5.0	1.69	1.11×10^{-11}
0.009	3.4	310	1.9	1060	4.6	1.59	1.11×10^{-11}
0.0095	3.4	308	1.9	1050	4.5	1.59	1.11×10^{-11}
0.011	3.5	303	1.9	1060	4.5	1.69	1.11×10^{-11}
0.02	4.2	313	1.9	1320	5.8	2.43	1.11×10^{-11}
0.021	4.1	289	1.9	1190	4.8	2.32	1.11×10^{-11}

liquid velocity) to become uniform, which was confirmed by measurement. The aspect ratio of the circular cylinder is $L/D = 12.0$ and 8.0, respectively, which is sufficiently large to guarantee the two-dimensionality of the flow. There is no average liquid flow through the tank and thus the three-dimensional effect as a result of interference by the tank wall is not sufficiently strong to disturb the measurement at the midspan. The corresponding blockage ratio is less than 4.5% and no correction for the blockage effect is applied to the measured data [33].

At the bottom of the tank, 55 spargers with 100 μm pores (SM-02, SANG-A Pneumatic Co., Ltd.) are installed in a square arrangement (11×5 configuration and the distance between adjacent spargers is 55 mm) [Fig. 1(a)] to introduce a homogeneous bubble swarm. The air pressure is varied through two successive regulators in the range 0–0.4 MPa, to control the flow rate, i.e., the void fraction. As a result, the volume void fraction (measured upstream of the circular cylinder) is varied from 0.3% to 2.1% and the average bubble diameter is 3.7 ± 0.3 mm. To regulate the inlet bubble condition more precisely, the airflow into each sparger is controlled independently by using a set of in-line regulators and solenoid valves. Thus, the bubble generation ensures the generation of a uniform bubble swarm without large-scale liquid recirculation (see Sec. III for the details).

B. Two-phase particle image velocimetry

It is important to measure the gas- and liquid-phases simultaneously to understand their interactions around the bluff body. To achieve this, we use two-phase high-speed particle image velocimetry, as shown in Fig. 1(b). The advantage of this method is the ability to capture the temporal and spatial variations of both phases in the instantaneous flow fields (i.e., visualization) in addition to the time-averaged flow statistics. To briefly summarize the method, a high-speed camera (NX5-S2, IDT vision) with a 50 mm lens (Nikon AF NIKKOR 1.8D) captures the images of both the gas- and liquid-phases at 1000 Hz with a resolution of 1680×1088 pixels, illuminated by two light sources. With the present setup, the depth of field (DoF) is calculated as $\mathrm{DoF} = sf^2/[f^2 - Nc(s-f)] - sf^2/[f^2 + Nc(s-f)] \simeq 8.0$ mm, which is approximately twice that of the average bubble size [Table I]. Here, the distance between the lens and measurement plane is $s = 800$ mm, $N = 1.8$, focal length $f = 67$ mm, and the circle of confusion is $c \simeq 0.017$ mm. As we explain in Sec. II C, we proceeded carefully to identify the in-focus bubbles accurately, but concede that the finite DoF may affect the gas-phase statistics. By changing the thresholds of binarization for edge detection, we confirmed that the influence is not significant (see below for more details about the uncertainty analysis). For the gas phase, continuous plane LED (red-colored, wavelength of 675 nm) is used to produce bubble shadow images, while a green laser sheet (wavelength of 532 nm) from a 5 W diode-pumped solid state (DPSS) continuous (CW) laser (RayPower 5000, Dantec Dynamics) is used to illuminate the seeders for the liquid flow. For the seeding particles, we use fluorescent particles (PMMA Rhodamine-B, sized 1–20 μm). At the opposite side of the laser, a mirror with a high reflective index is placed to minimize the blocking effect resulting from rising bubbles. An in-house calibration target is used to ensure that the incident and reflected laser

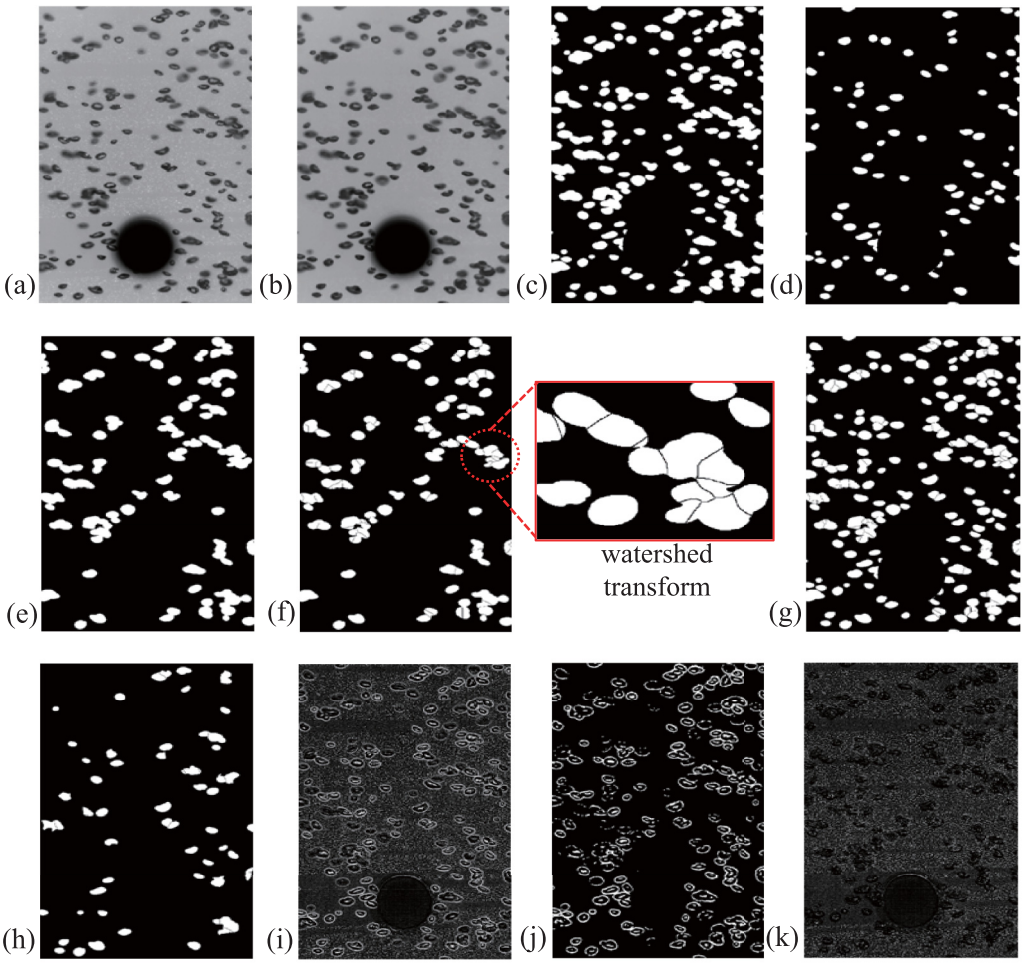

FIG. 2. Image processing sequence to discriminate gas (h) and liquid (k) phases from a raw image (a) obtained by a two-phase particle image velocimetry.

sheets are focused on the same plane. The high-speed camera is equipped with an orange filter (cutoff wavelength of 570 nm) such that the fluorescence of tracking particles (dominantly 576 nm, in water) is transmitted with the LED light (675 nm), while blocking the CW laser (532 nm) and associated reflections on the bubble surfaces. Figure 2(a) shows a representative raw image that was obtained with the present setup. The bubble shadows, seeding particles, and background clearly have different gray-scale values that can be distinguished with image processing.

From a raw image [Fig. 2(a)], two gray-scale intensity fields representing the gas and liquid phases can be obtained (see Sec. II C). The image of the seeding particles is then evaluated to measure the liquid velocity by the cross-correlation algorithm based on fast Fourier transform (with an interrogation window of 32 × 32 pixels, 75% overlap). When outliers of which the magnitudes are larger than three times of the standard deviation of spatially averaged velocity are detected, they are replaced by vectors that are interpolated from the neighboring 3 × 3 grids. In the resulting liquid-phase velocity fields, the spatial resolution is approximately 0.6 mm ($\sim 0.029D$ or $0.15\langle \bar{d}_b \rangle$). However, the bubble velocity is determined by calculating the distance traveled by individual bubble centroids, using a typical particle tracking velocimetry (PTV) algorithm that matches the closest neighboring bubble in the presumed direction of bubble motion [28]. In the measurement plane, the

centroids of each bubble are calculated from the planar projection of bubble images. Calculation of the equivalent size and shape is explained in Sec. II D. The measurements are carried out upstream and downstream of the circular cylinder (both on the mid-span plane). The field of view (FoV) has a size of 90×70 mm^2 ($-2.25 \leqslant x/D \leqslant 2.25$ and $-4.0 \leqslant y/D \leqslant -0.5$) for the upstream and 80×120 mm^2 ($-2.0 \leqslant x/D \leqslant 2.0$ and $-1.5 \leqslant y/D \leqslant 4.5$, for $D = 20$ mm) for the downstream regions, respectively, with the origin at the center of the cylinder. For a larger D of 30 mm, the spatial resolution is slightly reduced to $0.024D$ ($\sim 0.18\langle \bar{d}_b \rangle$). The upstream measurements were performed 430 mm ($\sim 108\langle \bar{d}_b \rangle$) above the sparger-array. For each case, 60 000 instantaneous velocity fields were obtained in order to obtain fully converged time-averaged statistics for gas- and liquid-phases.

For particle image velocimetry measurements, the velocity vector (u_p) is obtained as $u_p = M\Delta s/\Delta t$ with a magnification factor (M), time difference (Δt) between two consecutive particle images, and particle displacement (Δs). Therefore, any sources of uncertainties involved in acquiring those values can affect the total percentage error $\delta(u_p)$, shown in the following relation [19,34,35]:

$$\delta(u_p) = \sqrt{\delta(M)^2 + \delta(\Delta s)^2 + \delta(\Delta t)^2}. \tag{1}$$

The uncertainty regarding the magnification factor, $\delta(M)$, is estimated from an image of the calibration target placed on the laser sheet (thickness $\sim$2 mm) prior to each set of measurements. It is calculated to be 1.8% with M of 71.9 μm/pixel and 89.3 μm/pixel for $D = 20$ mm and 30 mm, respectively. For the time separation, the high-speed camera operating at its interframe time of 1 μs provides an error of $\delta(\Delta t) \simeq 0.1\%$ (the time difference between two consecutive images is 1 ms). Last, the pixel resolution that universally affects the particle displacement is 0.1 pixel, and thus $\delta(\Delta s)$ is estimated as 1.81% and 2.67% for $D = 20$ mm and 30 mm, respectively. Therefore, the overall uncertainty in the liquid velocity measurement is calculated to be 2.5–3.2%.

When detecting an individual bubble from a planar projection shadow image (Sec. II C), the equivalent bubble size, aspect ratio, and void fraction could possibly vary depending on the choice of the global threshold for binarization. We checked that by varying the threshold (from 0.05 to 0.4) of an adaptive document image binarization method [36] used to detect the bubble edges, their values deviate within the ranges of 3.6%, 2.1%, and 1.5%, respectively. The position of bubble centroids varied within 1.0%. However, the displacement of a bubble is measured by matching the closest neighboring bubble in the estimated direction of bubble motion and we constrained the traveled distance of each bubble to less than $d_b/4$. This is because the diameters of a considered bubble on two successive images should not differ by more than 5% [28]. Thus, with the information of the bubble detection accuracy, the uncertainty in measuring the bubble velocity is approximately 15.1 mm/s, which is 3.9% of the mean bubble rise velocity.

C. Phase discrimination with image processing

Digital image processing for phase discrimination is carried out based on the fact that the gray-scale values corresponding to bubble shadows, tracking particles, and background are different. Figure 2 shows the typical images corresponding to each step in the present procedure [19,31,32]. To extract bubbles, a median filter (7×7 pixels, sufficiently larger than the tracer particle) is first applied to the raw image [Fig. 2(a)], by which the tracking particles are regarded as noise and are removed [Fig. 2(b)]. The median-filtered image is binarized by an adaptive document image binarization method where each image is considered as a collection of 100×100 subwindows [36]. After that, 3-pixel-wide borders along the bubble perimeter are eliminated to compensate for the blurred regions or reflections (i.e., over-estimated bubble size) on the bubble surfaces [Fig. 2(c)] [27,37].

To enhance the accuracy of the measured gas-phase statistics, it is important to reliably separate the overlapped bubbles into solitary ones, and we use a watershed transform algorithm, region-based segmentation method using distance transformation [38]. As shown in Fig. 2(b), overlapped bubbles have a kind of internal and external markers; the internal markers are brighter regions (known as

minima) inside of the bubbles, and the external markers are midway between the internal markers. We use both markers to process the median-filtered image such that the regional minima appear only in the marked locations: locally brighter regions inside the coalesced bubbles are binarized by a global thresholding algorithm [39], which automatically finds the optimal global threshold that maximizes the between-class variance in the image histogram. In addition, we use the shape factor to prevent nonoverlapped bubbles from being divided [40]. For each bubble in the binarized image [Fig. 2(c)], the overlapped bubbles are selected by calculating the shape factor (R_o), defined as the ratio of the projected perimeter to the inner area, indicating that R_o becomes larger if more bubbles overlap. As a result, nonoverlapped bubbles [Fig. 2(d)] are labeled as solitary bubbles, whereas the remaining overlapped bubbles [Fig. 2(e)] are further processed with watershed transformation using the binarized minima image as an input [Fig. 2(f)]. We repeated this process [Fig. 2(f)] with a stiffer threshold 2–3 times and bubble segmentations resulting from the last loop are finally combined with the nonoverlapped bubbles to complete the gas-phase information [Fig. 2(g)]. The bubbles in Fig. 2(g) include all of those that are in-focus and out-of-focus. Using the fact that in-focus bubbles have higher gradients in the gray-scale value at the bubble surface, a Sobel filter is applied to extract the bubbles captured on the measurement plane by calculating the discrete differences within a 3×3 grid [Fig. 2(h)]. Unless specified otherwise, the gas-phase statistics are calculated based on the in-focus bubbles only, to be consistent with the planar measurement of liquid-phase statistics.

For the liquid-phase, we apply a Laplacian of Gaussian (LoG) filter to the raw image by which both bubbles and tracking particles are emphasized but the background illumination is suppressed [Fig. 2(i)] [19,28,41]. This procedure smoothens the image (thus, reducing noise). By sharpening the image again, regions with a sharp gray-scale contrast are highlighted whereas those with nearly constant gray-levels are suppressed to zero. To evaluate the bubble-induced liquid velocity with the PIV algorithm, only the seeding particle images are required; hence, the bubble surface images must be removed from Fig. 2(i). Thus, a median filter is applied to the LoG-filtered image to extract the bubble boundaries [Fig. 2(j)]. The final liquid-phase image (i.e., the image of the tracking particles only) is acquired by subtracting the image of the bubble boundaries from the LoG-filtered image [Fig. 2(k)]. Through each image-processing step, we confirmed that the footprints of bubble edges do not remain to distort the liquid-phase velocity.

D. Characterization of the considered gas-phase

We consider different inlet volume void fractions (defined as the ratio of the total volume occupied by in-focus and out-of-focus bubbles to the volume of the FoV) as $\langle\bar{\alpha}\rangle = 0.003, 0.006, 0.009, 0.0095, 0.011, 0.02$, and 0.021. In this paper, we use the subscripts "b" and "l" to denote bubble and liquid, respectively, and the subscript "∞" denotes the variable measured at the upstream location. If not specified otherwise, then the velocities are absolute values measured in the laboratory frame and subscript "r" is used to denote the relative quantity. The bubble size (d_b) is determined by calculating the volume-equivalent bubble diameter of a spheroid as $d_b = (d_{\max}^2 d_{\min})^{1/3}$, where $d_{\max}$ and $d_{\min}$ are the lengths of the major and minor axes of the assumed ellipsoidal cross section, respectively. The upstream conditions of the gas phase being considered are summarized in Table I. As $\langle\bar{\alpha}\rangle$ increases, the mean bubble diameter ($\langle\bar{d}_{b\infty}\rangle$) increases slightly while its mean rise velocity measured upstream, $\langle\bar{v}_{b\infty}\rangle$, tends to decrease owing to enhanced bubble-bubble interactions. The average bubble aspect ratio ($\beta = d_{\max}/d_{\min}$) is the same for all cases. The important dimensionless parameters for the present bubbles are: Reynolds number, $\mathrm{Re} = \rho_l \langle\bar{v}_{b\infty}\rangle \langle\bar{d}_{b\infty}\rangle \mu_l^{-1}$, Eötvös number, $\mathrm{Eo} = g(\rho_l - \rho_g)\langle\bar{d}_{b\infty}\rangle^2 \sigma^{-1}$, Weber number, $\mathrm{We} = \rho_l \langle\bar{v}_{b\infty}\rangle^2 \langle\bar{d}_{b\infty}\rangle \sigma^{-1}$, and Morton number, $\mathrm{Mo} = g\mu_l^4(\rho_l - \rho_g)(\rho_l^2\sigma^3)^{-1}$ (ρ_l and ρ_g, density of water and air; σ, surface tension of water; g, gravitational acceleration).

Figures 3(a) and 3(b) show the probability density function (PDF) of the equivalent bubble diameter and bubble rise velocity at the upstream ($y/D = -1.5$) location. The Gaussian curves corresponding to the cases of lowest and highest $\langle\bar{\alpha}\rangle$ are plotted together for comparison. The level of asymmetry in the distribution is quantified by the skewness, a third moment of fluctuating values.

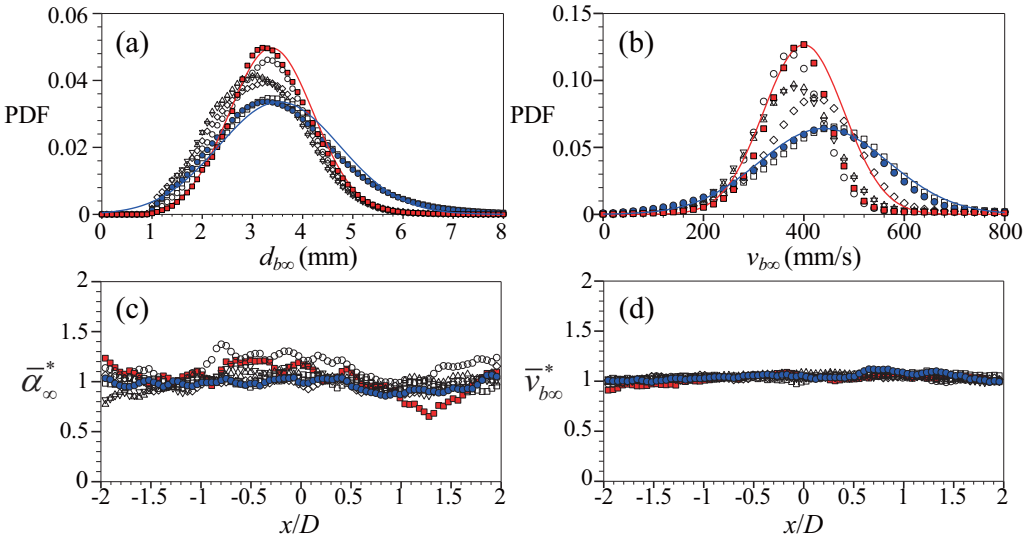

FIG. 3. Upstream ($y/D = -1.5$) condition of gas-phase: (a), (b) probability density function (PDF) of equivalent diameter (d_b) and rise velocity ($v_{b\infty}$) of bubbles; (c), (d) transverse distribution of local void fraction ($\bar{\alpha}_\infty$) and mean bubble rise velocity ($\bar{v}_{b\infty}$). ■, $\langle\bar{\alpha}\rangle = 0.003$; ○, 0.006; △, 0.009; ▽, 0.0095; ◇, 0.011; □, 0.02; ●, 0.021. Here, $*$ denotes the normalization with a global upstream value. In panels (a) and (b), solid lines denote the Gaussian curve for $\langle\bar{\alpha}\rangle = 0.003$ and 0.021, shown for comparison.

For $d_{b\infty}$, it is scattered in the range 0.17–0.51, without a specific trend with $\langle\bar{\alpha}\rangle$. For $v_{b\infty}$, the skewness gradually changes from 0.52 to −0.22, i.e., the distribution shifts to the right, as $\langle\bar{\alpha}\rangle$ increases from 0.003 to 0.021. This indicates that the acceleration due to bubble-bubble interaction becomes more probable with increasing $\langle\bar{\alpha}\rangle$. As we explained above, the uniform local void fraction [Fig. 3(c)] and streamwise bubble velocity [Fig. 3(d)] distributions are achieved along the transverse direction. However, we compared the measured terminal velocity of the present bubbles with that derived empirically [42]. This confirmed that the present bubbles more closely approximate the condition of a clean bubble rather than a fully contaminated one. Thus, no special correction was considered.

III. GAS-PHASE STATISTICS IN THE CYLINDER WAKE

The typical void distribution in the wake behind a circular cylinder (measured at $y/D = 1.5$) is shown in Fig. 4, for the case of $D = 20$ mm and $\langle\bar{\alpha}\rangle = 0.006$. Here, the superscript "*" denotes the normalization by the global upstream value, i.e., $\langle\bar{\bullet}_\infty\rangle$, and the time-averaged local void fraction, $\bar{\alpha}(x)$, is defined as the portion of bubble areas that exist on the two-dimensional measurement plane ($z/D = 0$). The figure compares the void distribution obtained by considering all the (in- and out-of-focus) bubbles, and they are almost the same. This comparison was repeated for other spanwise locations of $z/D = 1.5$, 3.0, and 4.5 (the chamber wall is $6D$ apart from the $z/D = 0$ plane). As shown, the void distribution shows a similar trend along the spanwise direction. Thus, the measurement on the center plane represents the present flow, and we discuss the results based thereupon.

Figures 5 and 6 show the contours of time-averaged void distribution ($\bar{\alpha}^*$) in the wake behind the circular cylinder of $D = 20$ mm and 30 mm, respectively, with $\langle\bar{\alpha}\rangle = 0.003$–0.021. In general, the rising bubbles collide in the front stagnation region of the cylinder, remain there for some time while bouncing several times, and then eventually slide along and separate from the cylinder surface. Thus, a region with a locally higher void fraction is established along these bubble trajectories. Based on

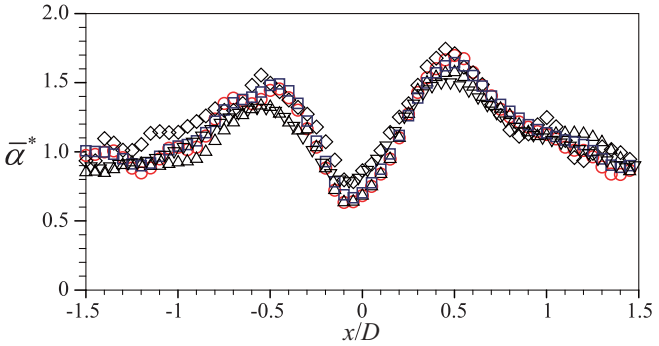

FIG. 4. Typical void ($\bar{\alpha}^*$) distributions in the wake ($y/D = 1.5$) behind a circular cylinder for $\langle\bar{\alpha}\rangle = 0.006$: □, at $z/D = 0$ (in-focus bubbles); ○, $z/D = 0$ (all bubbles); ◇, $z/D = 1.5$ (in-focus bubbles); △, $z/D = 3.0$ (in-focus bubbles); ▽, $z/D = 4.5$ (in-focus bubbles).

the variations in $\bar{\alpha}$, it is possible to classify two flow regimes: regime I in which two layers of higher $\bar{\alpha}$ develop along the location of separating shear layers ($|x/D| = 0.5$–0.7) and regime II in which the bubbles tend to concentrate behind the cylinder base ($x/D = 0$) as the layers of higher $\bar{\alpha}$ are deflected toward the centerline as the flow develops. For $D = 20$ mm ($\langle\bar{d}_b\rangle/D = 0.2$), the transition from regime I to II occurs at $\langle\bar{\alpha}\rangle \simeq 0.009$ [Fig. 5]. In regime I, a region of lower void fraction ($\bar{\alpha}^* < 1.0$) appears behind the cylinder ($-0.4 \lesssim x/D \lesssim 0.4$) and is sustained far downstream, but it is substantially reduced and disappears at $y/D \gtrsim 2.0$ in regime II. At $y/D \gtrsim 2.0$, a region with a higher bubble concentration ($\bar{\alpha}^* > 1.0$) appears; however, the void distribution rapidly becomes uniform because of enhanced mixing. These two regimes are clearly distinguishable from the streamwise profile of void fraction in the cylinder wake: from the base of cylinder ($y/D = 0.5$), $\bar{\alpha}^*$ slowly increases and saturates downstream in regime I; however, it increases sharply to the maximum in

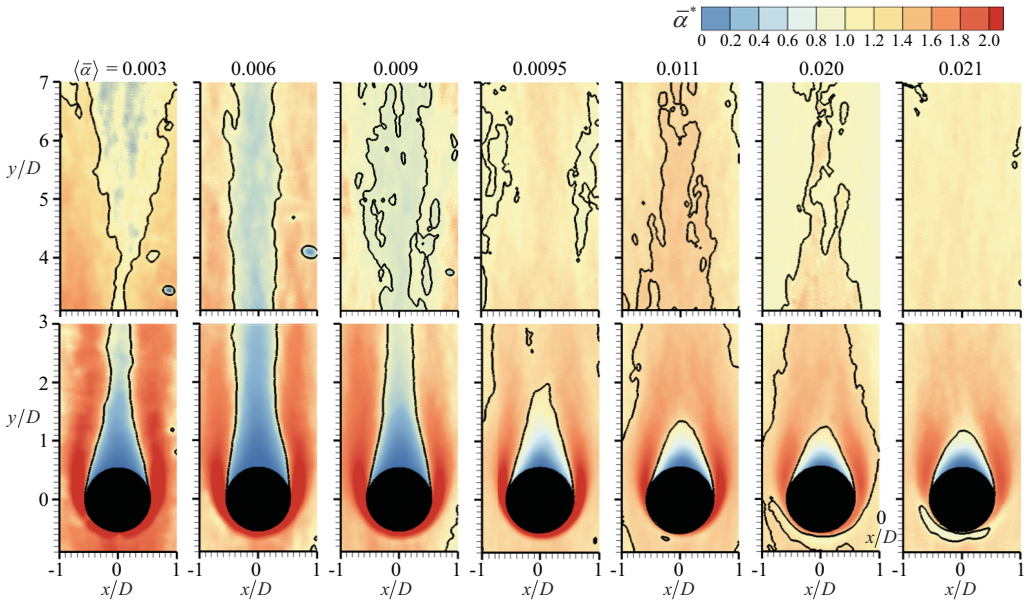

FIG. 5. Contours of time-averaged void ($\bar{\alpha}^*$) distributions in the cylinder ($D = 20$ mm) wake. In the contour, the solid lines denote the value of $\bar{\alpha}^* = 1.0$.

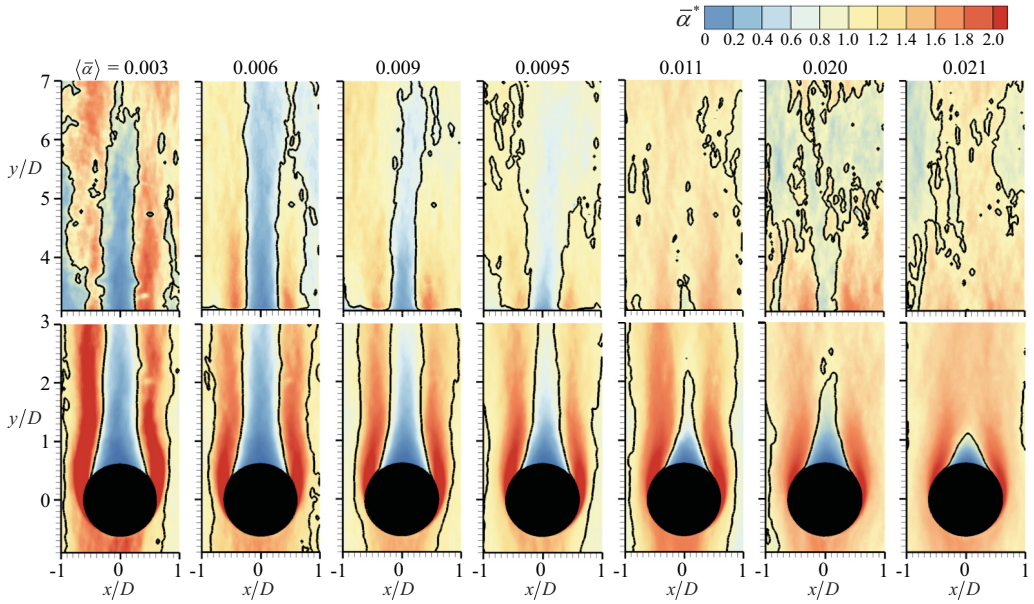

FIG. 6. Contours of time-averaged void ($\bar{\alpha}^*$) distributions in the cylinder ($D = 30$ mm) wake. In the contour, the solid lines denote the value of $\bar{\alpha}^* = 1.0$.

the near wake and gradually decreases to a saturated value in regime II. The same trend is observed as the diameter of the cylinder increases to $D = 30$ mm [Fig. 6]. However, the area of higher bubble concentration is reduced and the uniform void distribution is recovered farther downstream. This is because the effective bubble size ($\langle\bar{d}_b\rangle/D = 0.13$) is reduced and the cylinder wake width has increased. Here, the transition between the two regimes occurs at $\langle\bar{\alpha}\rangle \simeq 0.011$. Roughly speaking, the similar void distribution to that in regime II is found in previous studies [24,26], but the details show quite a different trend due to the existence of background flow and much higher void fraction (up to 25%) in those studies.

In Fig. 7, the transverse distribution of $\bar{\alpha}^*$ is plotted for the selected cases. As the flow passes around the cylinder, the void fraction profile is deflected such that the maximum (minimum) peaks are behind the cylinder edge (base) [Figs. 7(a) and 7(d)]. Because of enhanced bubble dispersion as a result of flow mixing, the magnitudes of peaks and valleys are saturated as the flow develops. For $D = 20$ mm (at $y/D = 1.5$), a minimum valley ($\bar{\alpha}^* \ll 1.0$) is observed at $x/D = 0$ and two distinctive peaks exist near a separating shear layer ($x/D = \pm 0.5$) for the cases of $\langle\bar{\alpha}\rangle = 0.003$, 0.009, and 0.011, but a broad peak appears (without a valley) for $\langle\bar{\alpha}\rangle = 0.021$ [Fig. 7(b)]. As the flow develops downstream (at $y/D = 2.5$), bubbles migrate toward the center of the cylinder and the case of $\langle\bar{\alpha}\rangle = 0.011$ also has a broad peak (transition to regime II) [Fig. 7(c)]. As $\langle\bar{\alpha}\rangle$ increases in regime II, the two peaks merge increasingly faster, but this is not observed in regime I, even far downstream of $y/D \simeq 10.0$. Beyond this, the bubbles disperse more or less uniformly, i.e., the effect of the circular cylinder disappears. In regime II, the shear-induced lift ($\vec{F}_L = -C_L\rho_l(\vec{v}_b - \vec{v}_l) \times (\nabla \times \vec{v}_l)$ [43]) increases drastically due to the intensified shear in the liquid flow ($y/D < 2.0$) (see Figs. 18 and 19) and the added-mass (due to the gradient of x-component of relative bubble velocity) and pressure gradient forces also act in the same direction, resulting in a preferential concentration of bubbles behind the cylinder. Here, $\vec{v}_b$ and $\vec{v}_l$ are bubble and liquid velocity vectors, respectively, and C_L is the lift coefficient. In regime I, however, $|\vec{v}_l|$ and its gradient is smaller and thus the drag force ($\vec{F}_D = C_D\rho_l(3/4d_b)|\vec{v}_r|\vec{v}_r$, C_D: drag coefficient) which is proportional to the square of the relative velocity ($\vec{v}_r = \vec{v}_b - \vec{v}_l$) of the bubble, becomes dominant (more than two times larger than regime I) to counteract the migration of the bubbles toward the center. For $D = 30$ mm, two

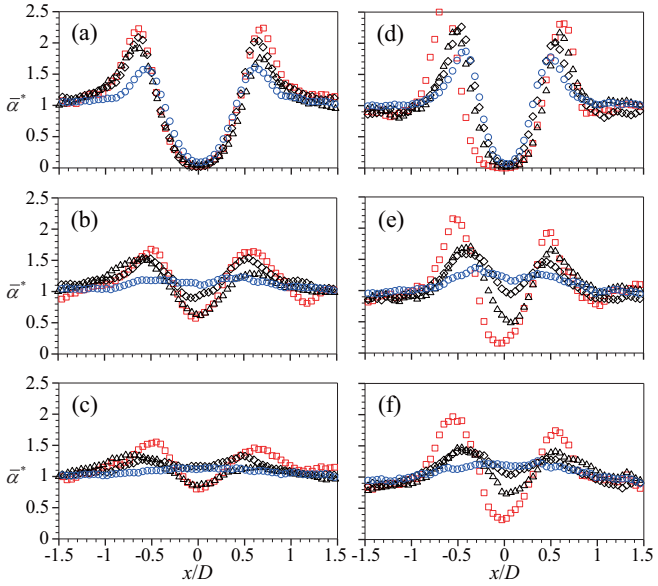

FIG. 7. Transverse distribution of local void fraction ($\bar{\alpha}^*$) at (a), (d) $y/D = 0.65$; (b), (e) 1.5; (c), (f) 2.5 behind the cylinder of (a)–(c) $D = 20$ mm and (d)–(f) 30 mm: □, $\langle\bar{\alpha}\rangle = 0.003$; △, 0.009; ◇, 0.011; ○, 0.021.

local maximum peaks are still observable for $\langle\bar{\alpha}\rangle = 0.021$ at $y/D = 1.5$ [Fig. 7(e)], and a single broad peak forms farther downstream of $y/D \gtrsim 2.5$ [Fig. 7(f)]. This is because the dispersion of bubbles occurs relatively slowly due to smaller $\langle\bar{d}_b\rangle/D$. Furthermore, the magnitudes of local peaks are larger, as the interfacial forces (such as drag and lift force) increase with enhanced disturbance (i.e., steeper shear) by the cylinder. Since it is challenging to achieve a thorough force analysis due to the inherent limitation in PIV resolution, we roughly compared and explained the dominating force components in each regime as did by Refs. [19,32,44]. The detailed mechanism of preferential bubble behaviors may be understood in terms of the instantaneous interfacial forces, for example, by solving the exact balance equations for each phase with the direct numerical simulation that can sufficiently resolve the forces acting on phase interfaces [45].

The interfacial forces acting on rising bubbles are strongly affected by their size (d_b) and aspect ratio (β) [46–48] and their transverse distributions in the wake are shown in Figs. 8 and 9, respectively. As shown in Figs. 8(a) and 8(d), larger (smaller) bubbles (than the mean bubble size) are found at $x/D \simeq \pm 0.5$ ($x/D \simeq 0$), right behind the cylinder. Because the bubble-induced liquid flow evolves into a steeper velocity gradient (wake defect) behind the cylinder (see Sec. IV), smaller bubbles are attracted to the lower velocity region (i.e., toward $x/D = 0$) while larger bubbles accumulate behind the cylinder sides ($x/D \simeq \pm 0.5$). As the flow develops the uniformity in bubble size distribution recovers rapidly, which is faster for the case of larger $\langle\bar{d}_b\rangle/D$ (smaller D) [Figs. 8(c) and 8(f)]. Interestingly, the bubble size saturates faster than the void fraction. This is because the transverse migration of bubbles (i.e., the shear-induced lift force) is directly affected by the bubble size; however, the void distribution is determined by both the size and frequency of the bubbles.

In addition, the distribution of β can be understood in relation to void distribution [Fig. 9]. The present bubble aspect ratio is in the range $\beta = 1.3$–2.1. Along the transverse direction, the aspect ratio remains to be almost constant at $|x/D| > 0.5$, but decreases sharply toward the cylinder base [Figs. 9(a) and 9(d)]. As the flow develops, the aspect ratio also shows a uniform distribution. Interestingly, unlike the void fraction and bubble size, the convergence of $\bar{\beta}$ occurs faster for the case of larger D [Figs. 9(b) and 9(e)]. This is related to the dependency on β of the shear-induced lift force on a rising bubble. Previously, Adoua *et al.* [48] simulated the flow around an oblate

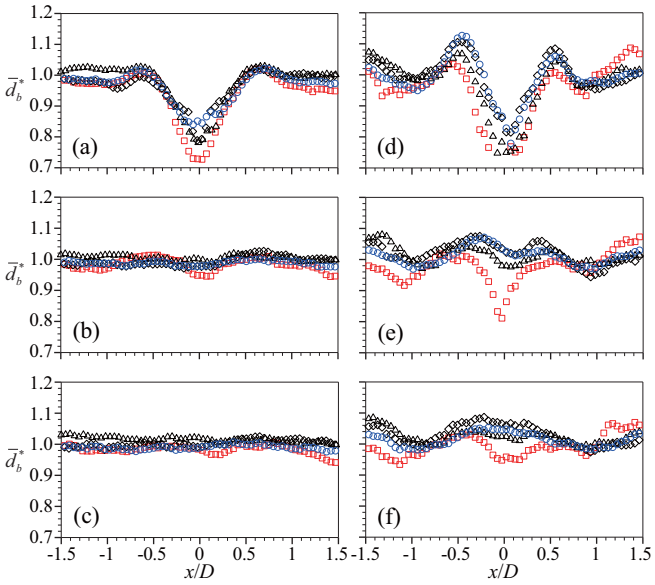

FIG. 8. Transverse distribution of equivalent bubble diameter ($\bar{d}_b^*$) at (a), (d) $y/D = 0.65$; (b), (e) 1.5; (c), (f) 2.5 behind the cylinder of (a)–(c) $D = 20$ mm and (d)–(f) 30 mm: □, $\langle\bar{\alpha}\rangle = 0.003$; △, 0.009; ◇, 0.011; ○, 0.021. Here, $*$ denotes the normalization with a global upstream value, $\langle\bar{d}_{b\infty}\rangle$.

spheroidal bubble under different conditions and showed that the sign of the lift force changes with β for Re $= \boldsymbol{O}(10^2$–$10^3)$, under a relatively weak shear rate. According to them, the bubble moves toward the higher liquid velocity region when $\beta \lesssim 2.2$ (lift force increases with increasing

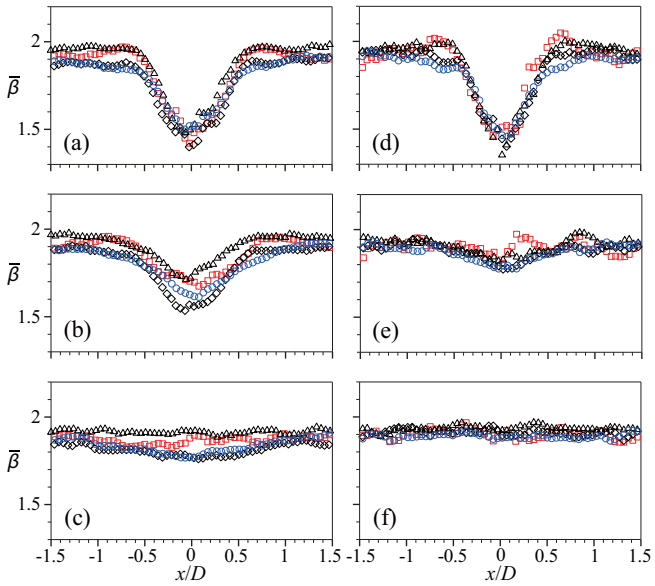

FIG. 9. Transverse distribution of bubble aspect ratio ($\beta = d_h/d_v$) at (a), (d) $y/D = 0.65$; (b), (e) 1.5; (c), (f) 2.5 behind the cylinder of (a)–(c) $D = 20$ mm and (d)–(f) 30 mm: □, $\langle\bar{\alpha}\rangle = 0.003$; △, 0.009; ◇, 0.011; ○, 0.021.

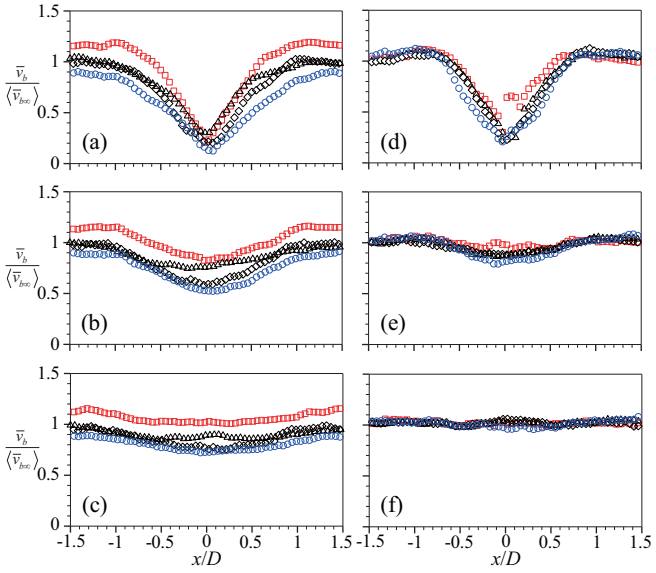

FIG. 10. Transverse distribution of mean bubble rise velocity ($\bar{v}_b$), normalized by $\langle \bar{v}_{b\infty} \rangle$, at (a), (d) $y/D =$ 0.65; (b), (e) 1.5; (c), (f) 2.5 behind the cylinder of (a)–(c) $D = 20$ mm and (d)–(f) 30 mm: □, $\langle \bar{\alpha} \rangle = 0.003$; △, 0.009; ◇, 0.011; ○, 0.021.

β), which is reversed at $\beta \gtrsim 2.2$. For the present cases (the dimensionless shear-rate ($\lesssim$0.2) is small and Re $\simeq$ 1100), the bubble aspect ratios are below 2.0, thus more deformed (i.e., higher β) bubbles would have a higher possibility to move out of the wake defect region which is, as a result, populated by bubbles with a lower β. As the diameter of the cylinder increases, the velocity gradient behind the cylinder becomes steeper and is retained longer in the wake (Figs. 18 and 19). Thus the contribution of the shear-induced lift force is stronger and causes the bubble aspect ratio distribution to converge faster.

Finally, the streamwise ($\bar{v}_b$) and transverse ($\bar{u}_b$) velocities of bubbles are compared in Figs. 10 and 11, respectively. The streamwise velocity has a minimum valley behind the cylinder, which gradually recovers the upstream value along the streamwise direction [Figs. 10(c) and 10(f)]. The transverse velocity (below 40% of the rise velocity in maximum value) shows a skew-symmetric profile centered at the origin, and the peak values (at $|x/D| = 0.1$–0.2) decrease and the corresponding locations are shifted away from the centerline with increasing $\langle \bar{\alpha} \rangle$ (Fig. 11). At $-0.5 < x/D < 0.5$, the bubble rise velocity increases but the transverse component decreases as the flow develops, which is associated with lateral movements of the bubbles promoted closer to the cylinder base [Figs. 11(a) and 11(d)], where the liquid-phase velocity gradient is steeper. The transverse velocity diminishes fast as the bubbles rise away from the cylinder [Figs. 11(c) and 11(f)]. As the cylinder diameter increases, the overall trend of the bubble velocity distribution is not affected but the deviation between different $\langle \bar{\alpha} \rangle$'s is reduced. This is because the hydrodynamic influence of bubbles is reduced by the smaller $\langle \bar{d}_b \rangle / D$, and thus a larger increase in $\langle \bar{\alpha} \rangle$ is required to obtain a distinctive difference in the bubble velocity for a larger cylinder. However, it was shown that the mean bubble rise velocity and relative rise velocity is proportional to $\langle \bar{\alpha} \rangle^{-0.1}$ for a bubble swarm in quiescent water ($0.005 \leqslant \langle \bar{\alpha} \rangle \leqslant 0.1$) [8] and for an upward laminar bubbly pipe flow ($0.0005 \leqslant \langle \bar{\alpha} \rangle \leqslant 0.0064$) [19], respectively. In the present cases, the scaling relation is satisfied to some extent in the upstream and downstream ($|x/D| > 0.5$) regions (Fig. 12), but the existence of the circular cylinder slightly disturbs the void fraction dependency at $|x/D| < 0.5$ in the downstream region.

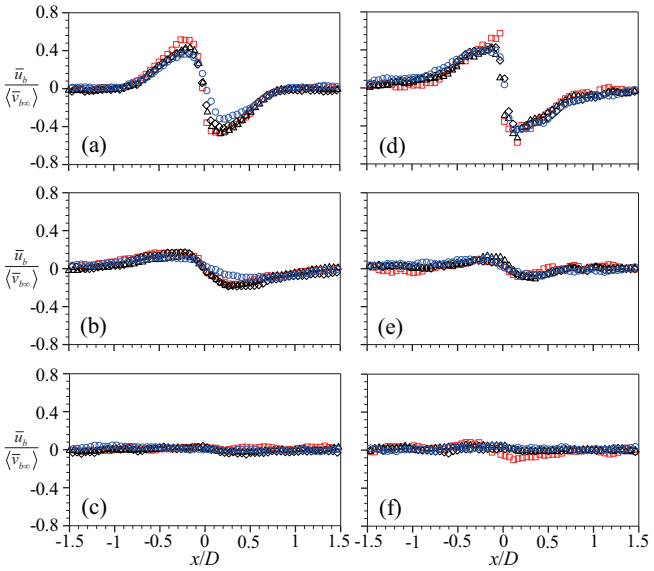

FIG. 11. Transverse distribution of mean bubble transverse velocity ($\bar{u}_b$), normalized by $\langle \bar{v}_{b\infty} \rangle$, at (a), (d) $y/D = 0.65$; (b), (e) 1.5; (c), (f) 2.5 behind the cylinder of (a)–(c) $D = 20$ mm and (d)–(f) 30 mm: □, $\langle \bar{\alpha} \rangle = 0.003$; △, 0.009; ◇, 0.011; ○, 0.021.

IV. BUBBLE-INDUCED LIQUID FLOW AROUND A CIRCULAR CYLINDER

A. Characterization of the upstream flow

In this section, we discuss the quantitative flow statistics for the liquid phase measured upstream. Based on our identification of two flow regimes, we measure the bubbly flows for the cases of $\langle \bar{\alpha} \rangle = 0.006$ and 0.011 for both $D = 20$ mm and 30 mm, representing regimes I and II, respectively. The time-averaged liquid velocity at the upstream ($y/D = -1.5$) location is shown in Fig. 13. Here, the velocities are nondimensionalized by $\langle \bar{v}_{b\infty} \rangle$. As can be expected from the void distribution (Fig. 3),

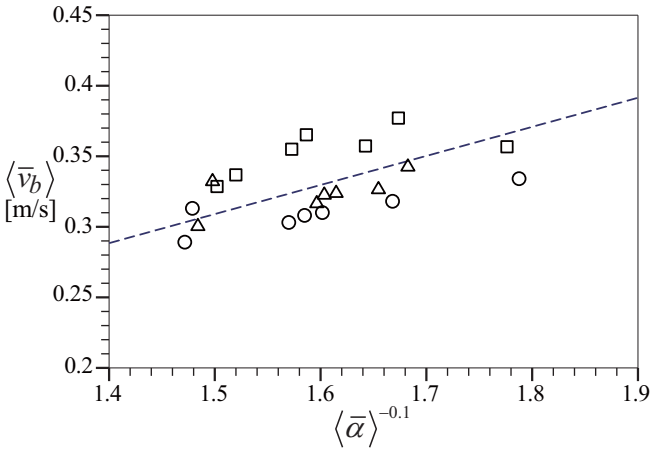

FIG. 12. Scaling relation between mean bubble rise velocity and $\langle \bar{\alpha} \rangle$: ○, measured at upstream; △, outside of the nearwake ($|x/D| > 0.5$) for $D = 20$ mm; □, 30 mm.

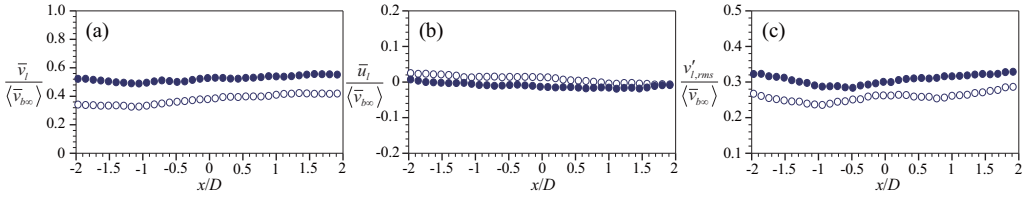

FIG. 13. Upstream ($y/D = -1.5$) bubble-induced liquid flow: (a) mean streamwise velocity ($\bar{v}_l$); (b) mean transverse velocity ($\bar{u}_l$); (c) root-mean-square of streamwise velocity fluctuation ($v'_{l,\mathrm{rms}}$); ○, $\langle\bar{\alpha}\rangle = 0.006$; ●, 0.011.

the upstream liquid-phase velocity is more or less uniform throughout the measurement area. As $\langle\bar{\alpha}\rangle$ increases, the mean streamwise liquid velocity becomes faster (approximately $0.52\langle\bar{v}_{b\infty}\rangle$) [Fig. 13(a)] due to the enhanced bubble-bubble interaction. The transverse velocity is almost negligible in a time-averaged sense [Fig. 13(b)]. Although the transverse bubble velocity exists in instantaneous flows due to the oscillating path of an individual bubble, these flows are mitigated by the homogeneous bubble distribution.

As is well known, a substantial level of velocity fluctuation (so-called bubble-induced turbulence or agitation) is also induced by the present bubbles, which increases with increasing $\langle\bar{\alpha}\rangle$ [Fig. 13(c)]. To investigate the turbulent nature of the bubble-agitated upstream flow, we examine the PDF of liquid-phase velocity measured at $-4.0 \leqslant y/D \leqslant -0.5$ (Fig. 14). The streamwise velocity fluctuation shows non-Gaussian behavior: the PDF is observed to exhibit positive skewness, due to the stronger entrainment of the liquid flow into the bubble wake [2,5,8,13]. Moreover, the PDF tends to exhibit exponential decays (with a linear slope on the semilog-axes graph). The transverse velocity fluctuation, however, shows symmetric behavior, which does not change much with $\langle\bar{\alpha}\rangle$. This is because the bubble-induced liquid flow in the vicinity of zigzagging bubbles is axisymmetric on average and the transverse void distribution is also statistically uniform. Previously, Riboux *et al.* [8] showed that the root-mean-square (r.m.s.) of the liquid-phase velocity fluctuation is scaled with $\langle\bar{\alpha}\rangle^{0.4}$ in a homogeneous bubble-swarm, which was extended to the upward laminar bubbly flow [19]. Under the present conditions, it is found that the spatially averaged streamwise velocity fluctuation is $\langle v'_{l,\mathrm{rms}}\rangle/\langle\bar{v}_{b\infty}\rangle \simeq 0.25$ and 0.33, for $\langle\bar{\alpha}\rangle = 0.006$ and 0.011, respectively, which is asymptotically scaled with $\langle\bar{\alpha}\rangle^{0.4}$ (see Fig. 23). In Sec. IV C, we discuss whether this correlation remains valid for the wake region behind the cylinder. The turbulence intensity ($\langle v'_{l,\mathrm{rms}}\rangle/\langle\bar{v}_l\rangle$) of

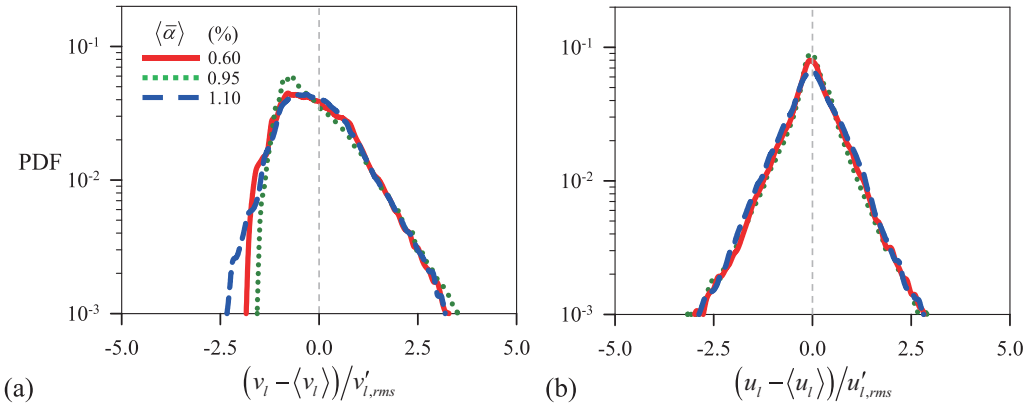

FIG. 14. Probability density function (PDF) of the liquid-phase velocity fluctuations in (a) streamwise and (b) transverse components, measured at the upstream ($-4.0 \leqslant y/D \leqslant -0.5$) of the circular cylinder.

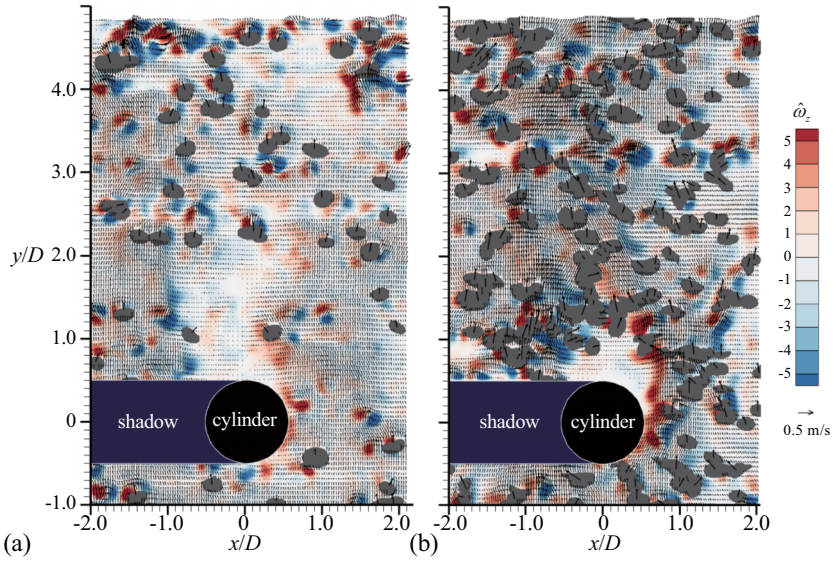

FIG. 15. Instantaneous two-phase flow with velocity vectors and contour of $\hat{\omega}_z$ around a circular cylinder ($D = 20$ mm): (a) $\langle\bar{\alpha}\rangle = 0.006$; (b) 0.011. Bubbles that are located on and in front of the $z/D = 0$ plane are shown.

the upstream liquid-phase flow is calculated to be approximately 0.71 and 0.6, for $\langle\bar{\alpha}\rangle = 0.006$ and 0.011, respectively. Based on the PDF of the liquid-phase velocity fluctuation and scaling in relation to $\langle\bar{\alpha}\rangle$, we consider the bubble-induced agitation in the upstream region corresponds to that of a homogeneous swarm of rising bubbles [2,13].

B. Bubble-induced flow in the cylinder wake

Figures 15 and 16 show instantaneous flow fields representing each flow regime ($\langle\bar{\alpha}\rangle = 0.006$ and 0.011) in the cylinder wake ($-1.0 \leqslant y/D \leqslant 4.0$). For the present cases, bubbles mostly rise in two-dimensional zigzag paths (or sometimes take three-dimensional helical motions), which are expected from the dimensionless numbers (Table I). Even downstream of the circular cylinder, most of the bubbles were observed to rise in a two-dimensional plane by tracking the center positions of each bubble. For regime I ($\langle\bar{\alpha}\rangle = 0.006$), bubbles are hardly observed in the near-wake region ($y/D < 2.0$), and thus bubble-induced liquid flow is relatively weak there [Fig. 15(a)]. Because the rising bubbles induce spatially nonuniform flow instantaneously, the organized evolution of a separating shear layer behind the cylinder is not clearly observed. As the flow continues to develop, the uniform distribution of the bubbles is restored. Similar to the upstream flow, the individual bubble wake structure is sustained for a certain period of time. As $\langle\bar{\alpha}\rangle$ increases to 0.011 (regime II), the near wake has a greater population of bubbles, inducing an enhanced shear flow (with an intensive turbulence, as well) behind the cylinder edge [Fig. 15(b)]. This strong shear in turn forces the trajectories of rising bubbles to deflect toward the center of the cylinder. It is also noted that bubble-induced flow structures become complex as the interaction between the bubble-wakes occurs more frequently. Although the overall difference between two regimes is maintained for the larger cylinder diameter, the enlarged wake width appears to affect the two-phase flow pattern (Fig. 16). For example, at $\langle\bar{\alpha}\rangle = 0.006$, more bubbles are entrained and rise along the separating shear layer, which would perturb the liquid-phase flow more frequently [Fig. 16(a)]. As shown in Figs. 7(d)–7(f), the rising bubbles disperse slowly and thus the higher concentration along the shear layer is sustained longer in the downstream. With $\langle\bar{\alpha}\rangle = 0.011$, the entrainment of the bubbles into the near

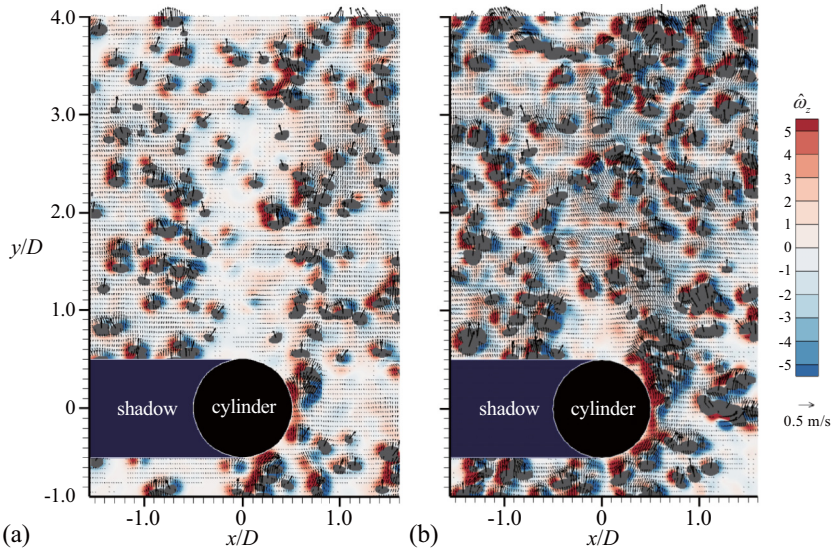

FIG. 16. Instantaneous two-phase flow with velocity vectors and contour of $\hat{\omega}_z$ around a circular cylinder ($D = 30$ mm): (a) $\langle\bar{\alpha}\rangle = 0.006$; (b) 0.011. Bubbles that are located on and in front of the $z/D = 0$ plane are shown.

wake region also becomes more vigorous, but the relative size of bubble-induced vortical structures compared to the cylinder size (D) is reduced [Fig. 16(b)].

The time-averaged spanwise vorticity ($\hat{\bar{\omega}}_z = \bar{\omega}_z D/\langle\bar{v}_b\rangle$) of the bubble-induced liquid flow is shown in Fig. 17, together with the contour of $\bar{\alpha}^*$. It is noted that the present wake behind the

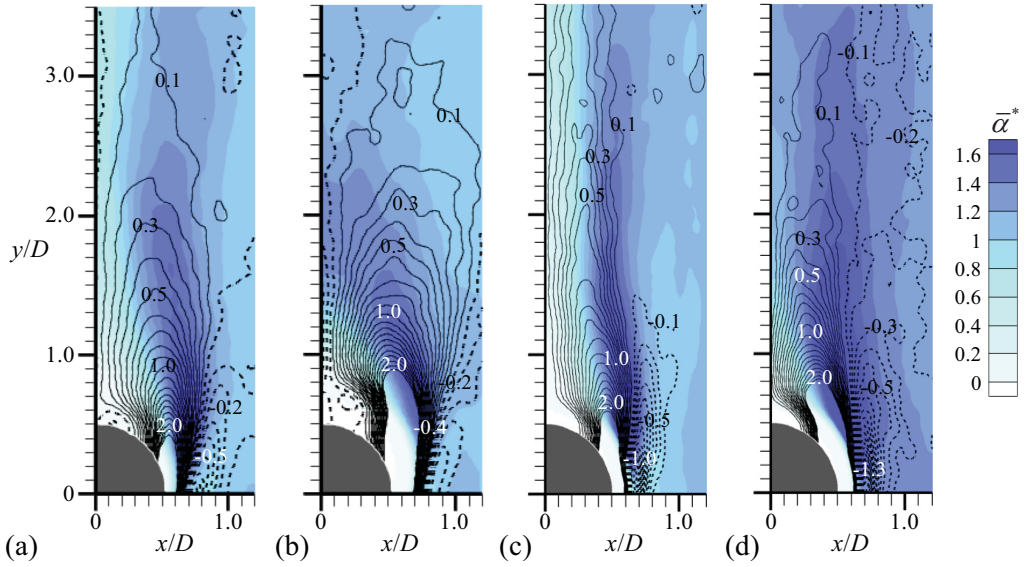

FIG. 17. Contours of time-averaged spanwise vorticity, $\hat{\bar{\omega}}_z$ (line) and local void fraction, $\bar{\alpha}^*$ (flood) in the wake behind the cylinder of (a), (b) $D = 20$ mm and (c), (d) 30 mm: (a), (c) $\langle\bar{\alpha}\rangle = 0.006$; (b), (d) 0.011. Here, the line contour levels are set in the increments of 0.1, and dashed lines denote negative value.

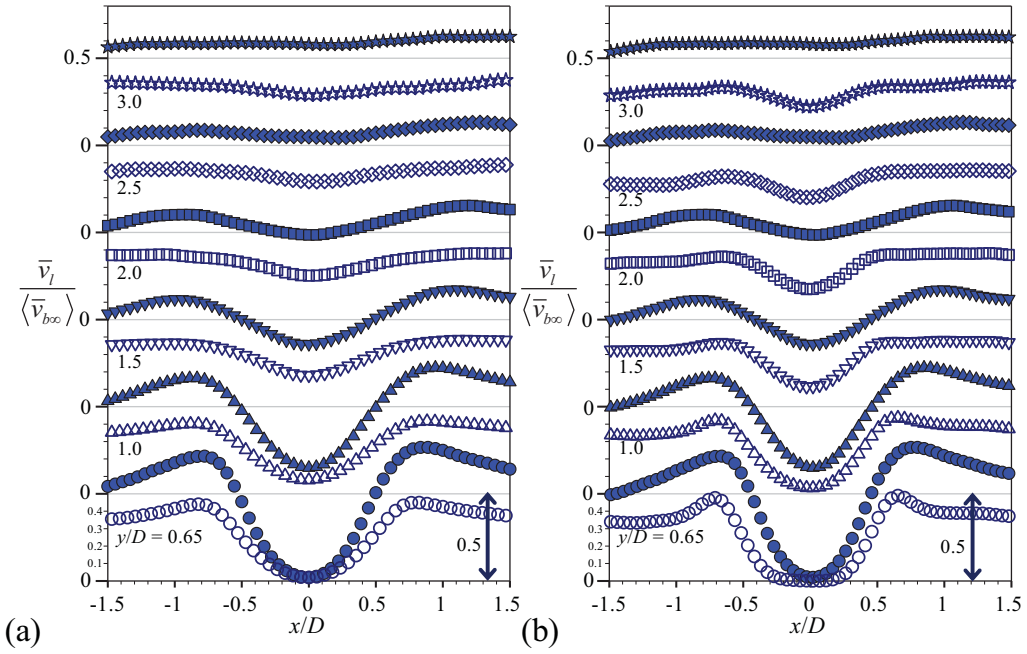

FIG. 18. Transverse distributions of the mean streamwise velocity ($\bar{v}_l$) of liquid phase in the wake behind a cylinder at $y/D = 0.65$ (○), 1.0 (△), 1.5 (▽), 2.0 (□), 2.5 (◇), and 3.0 (⋆): (a) $D = 20$ mm; (b) 30 mm. Open symbols, $\langle\bar{\alpha}\rangle = 0.006$; closed symbols, 0.011. In vertical axes, the size of minor ticks is 0.1 and some example values are given.

circular cylinder is in nature different from that of the single-phase wake flow because there is no initial mean liquid flow developed incident to the circular cylinder. Instead the liquid motion is solely induced by the bubble motions, generating an enhanced turbulence intensity in the flow as well. As the bubble-induced flow passes around the cylinder, a shear layer evolves from the cylinder edge ($x/D \simeq 0.5$). Interestingly, a secondary vortex structure (with an opposite sign of ω_z) is induced next to this main shear layer ($x/D = 0.7$–0.8). This secondary vortex structure becomes more elongated as $\langle\bar{\alpha}\rangle$ and D increase. To understand this, we compared the mean spanwise vorticity ($\hat{\bar{\omega}}_z$) and transverse gradient of the streamwise liquid velocity ($\partial\bar{v}_l/\partial x$) in the near wake (for example, at $y/D = 0.65$), and found that the magnitude and location of local peaks match well each other. Furthermore, the local void [$\bar{\alpha}(x)$] peaks are located between the main and secondary vortices. Thus, it is understood that the bubbles that rise along the cylinder surface generate regions with a higher void fraction near $x/D = 0.7$ and thus locally accelerates the liquid flow (higher shear is induced) in these locations, which leads to the evolution of the secondary vortex. As $\langle\bar{\alpha}\rangle$ increases, following the change in the void distribution, the higher vorticity region ($\hat{\bar{\omega}}_z \geqslant 2.0$) becomes wider along both the streamwise and transverse directions, and thus the location of maximum spanwise vorticity moves accordingly [Figs. 17(b) and 17(d)]. As D increases, the maximum void fraction increases and is observed farther downstream for both flow regimes. Therefore, the magnitude of bubble-induced $\bar{\omega}_z$ increases as well and the corresponding position is delayed into the downstream region [Figs. 17(c) and 17(d)].

Considering that bubble-induced liquid flow induces a specific flow structure around the cylinder, it would be interesting to investigate the detailed flow statistics resulting from bubble-induced flow. The streamwise variations in the time-averaged streamwise (v_l) and transverse (u_l) velocity profiles are shown in Figs. 18 and 19, respectively. As shown, the streamwise velocity shows a symmetric distribution that resembles that of a wake defect and the transverse component has a

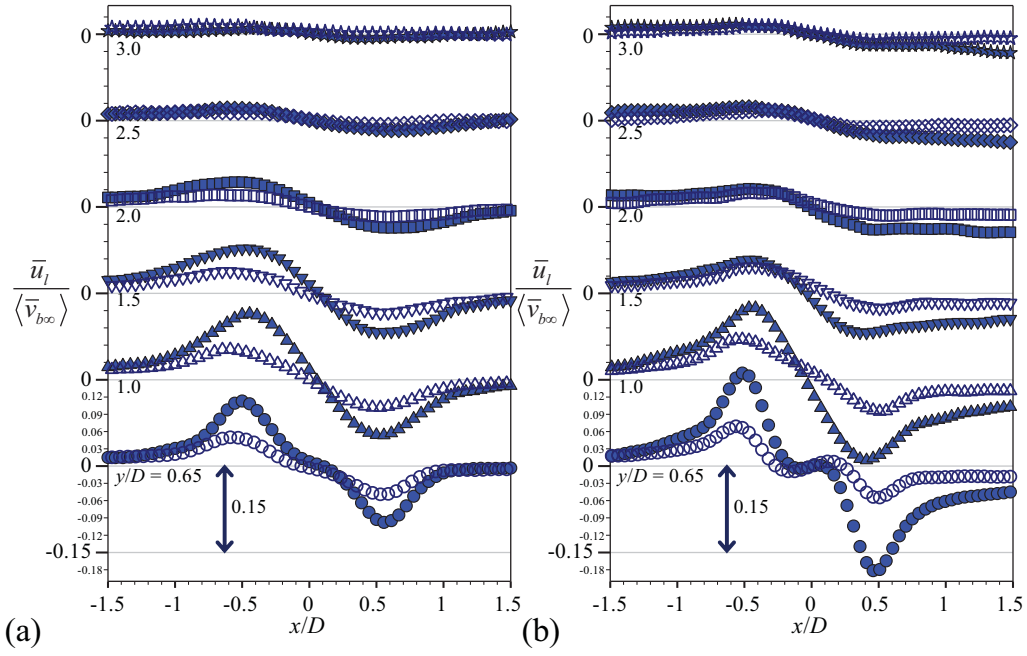

FIG. 19. Transverse distributions of the mean transverse velocity ($\bar{u}_l$) of liquid phase in the wake behind a cylinder at $y/D = 0.65$ (○), 1.0 (△), 1.5 (▽), 2.0 (□), 2.5 (◇), and 3.0 (⋆): (a) $D = 20$ mm; (b) 30 mm. Open symbols, $\langle\bar{\alpha}\rangle = 0.006$; closed symbols, 0.011. In vertical axes, the size of minor ticks is 0.03 and some example values are given.

skew-symmetric profile with peaks located along the shear layer, which flatten out fast as the flow develops. The liquid flow is locally accelerated in the presence of more bubbles ($x/D \simeq \pm 0.5$) but is decelerated where the void fraction is smaller ($x/D \simeq 0$). For both regimes, the streamwise velocity profile thus has two maximum and one minimum values in the near wake ($y/D \lesssim 2.0$) following the void distributions. However, the recovery of the downstream velocity deficit ($y/D \gtrsim 2.0$) is faster for regime II ($\langle\bar{\alpha}\rangle = 0.011$) owing to the enhanced bubble dispersion along the transverse direction (Fig. 18). As $\langle\bar{\alpha}\rangle$ increases, the bubble-induced liquid flow becomes faster from $0.35\langle\bar{v}_{b\infty}\rangle$ to $0.55\langle\bar{v}_{b\infty}\rangle$, and the velocity gradient near the cylinder edge becomes sharper. As the diameter of the cylinder increases, the bubble-induced velocity is accelerated even more, with a steeper gradient in the near wake. This is because more bubbles are entrained and shed into the downstream area in the form of bubble cluster, as shown in Figs. 15(b) and 16(b). In addition, this tendency is retained farther downstream and thus the recovery of the velocity deficit is delayed [Fig. 18(b)]. Compared to the streamwise velocity, the magnitude of the transverse velocity (u_l) is quite small, and shows an antisymmetric distribution with local peaks (along the separating-shear layers) where the bubbles are accumulated (Fig. 19). Similar to the streamwise velocity, higher u_l is induced as $\langle\bar{\alpha}\rangle$ increases, which is reduced significantly at $y/D > 2.0$. Even though the defect in the streamwise velocity is recovered faster in regime II, the convergence of the transverse velocity occurs faster in regime I, because of the slight preferential migration of bubbles along the transverse direction. This corresponds to the change in the void distribution (Fig. 7). For $D = 30$ mm, the velocity distribution has the same overall trend but the maximum peak of $\bar{u}_l$ increases and the slope of the velocity gradient becomes steeper, which is maintained longer downstream [Fig. 19(b)].

From the viewpoint of a circular cylinder, the Reynolds number for the liquid flow is in the range $\mathrm{Re}_D = \langle\bar{v}_l\rangle D/\nu = 2000$–$5000$, where ν is the kinematic viscosity of water. For a single-phase flow at this Re_D, the typical size of a recirculation bubble (the distance from the cylinder base to

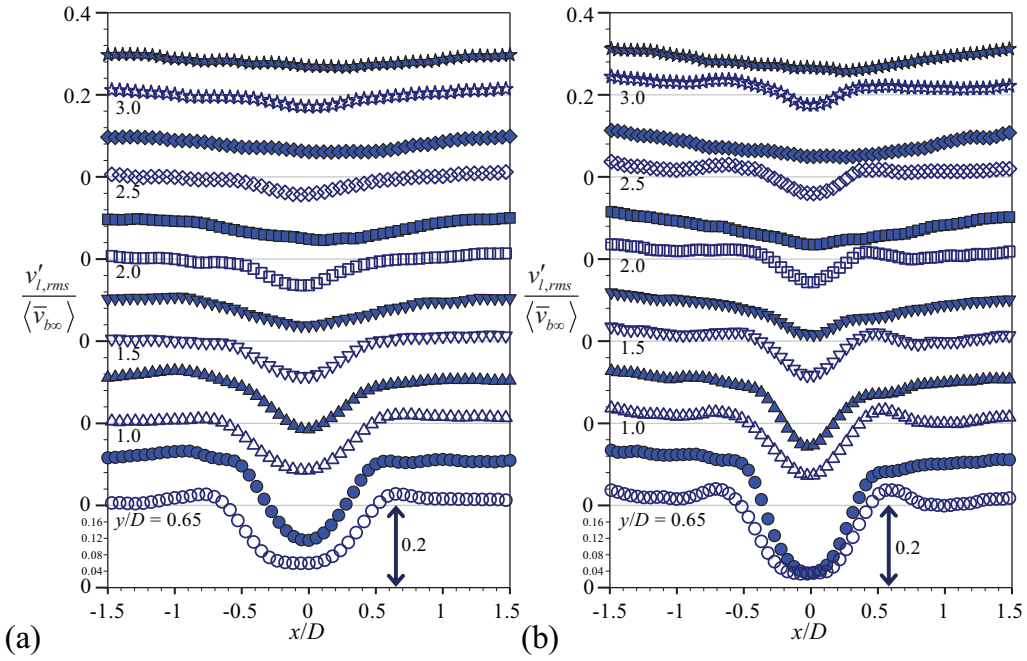

FIG. 20. Transverse distributions of the root-mean-square of streamwise velocity fluctuations ($v'_{l,\mathrm{rms}}$) of liquid phase in the wake behind a cylinder at $y/D = 0.65$ (○), 1.0 (△), 1.5 (▽), 2.0 (□), 2.5 (◇), and 3.0 (⋆): (a) $D = 20$ mm; (b) 30 mm. Open symbols, $\langle \bar{\alpha} \rangle = 0.006$; closed symbols, 0.011. In vertical axes, the size of minor ticks is 0.04 and some example values are given.

the location of the zero mean streamwise velocity on the centerline) has been reported as $l_r/D = 1.4$–1.5 [35]. For the present two-phase flows, it is measured to be $l_r/D \simeq 0.2$ for $\langle \bar{\alpha} \rangle = 0.011$, but is not clearly identifiable (i.e., no distinct region of backflow) for a lower void fraction case. This indicates that the extent to which the fluid is mixed by a bubbly flow is enhanced significantly compared to a single-phase flow. Because the surrounding water is initially static and the existence of bubbles affects the flow property (e.g., the effective viscosity and density change), the comparison would require more cautious analysis. However, it is understood that the highly enhanced turbulence in the upstream flow and the preferential migration of the bubbles behind the cylinder are responsible for the considerably reduced size of recirculation bubble in the wake.

C. Bubble-induced liquid fluctuation in the wake

Here, we discuss the way in which the bubble-induce turbulence is re-distributed owing to the existence of the bluff body. The root-mean-square values of velocity fluctuations in the streamwise ($v'_{l,\mathrm{rms}}$) and transverse ($u'_{l,\mathrm{rms}}$) directions are shown in Figs. 20 and 21, respectively, and the Reynolds stress ($-\overline{u'_l v'_l}$) profiles are plotted in Fig. 22. These show that a small fraction of bubbles generates a certain level of turbulence in the flow; because there is no background flow, the trends represent the nature of pure bubble-induced turbulence (agitation) around a solid body. As the upstream flow has quite a high level of turbulence, significant turbulence intensity is also measured outside of the cylinder ($|x/D| > 0.5$) (Figs. 20 and 21). The streamwise turbulence intensity shows a relatively simple distribution where it has a broad valley behind the cylinder ($-0.5 < x/D < 0.5$), following the void distribution. As the flow develops, this local minimum is reduced and the uniform distribution is restored like the upstream flow, which occurs slower with a lower $\langle \bar{\alpha} \rangle$ and larger D [Fig. 20]. As D increases [Fig. 20(b)], however, the turbulence level decreases slightly

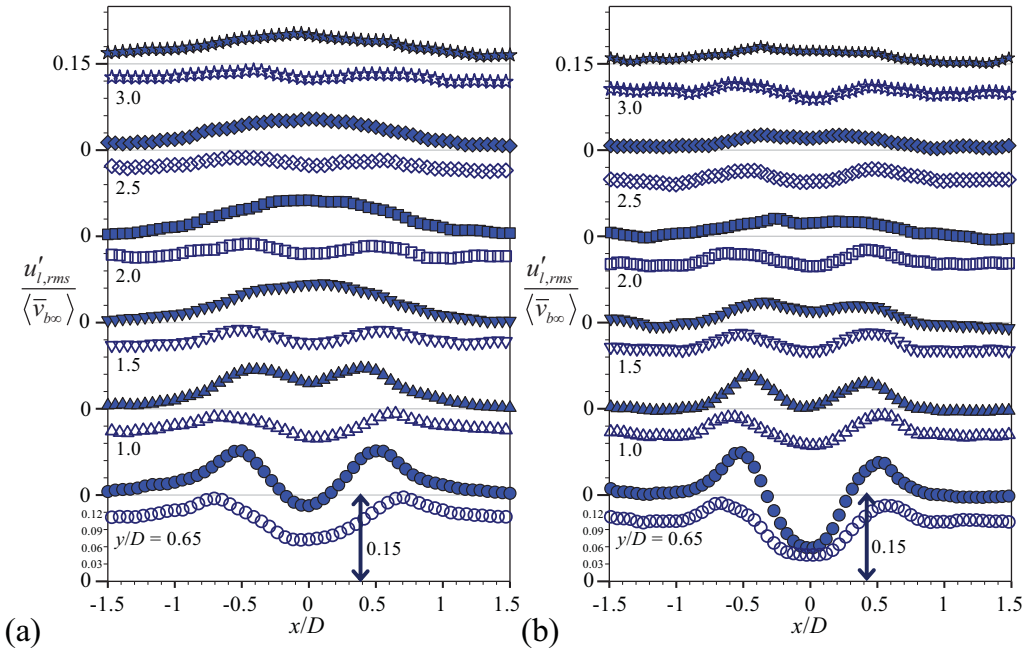

FIG. 21. Transverse distributions of the root-mean-square of transverse velocity fluctuations ($u'_{l,\mathrm{rms}}$) of liquid phase in the wake behind a cylinder at $y/D = 0.65$ (○), 1.0 (△), 1.5 (▽), 2.0 (□), 2.5 (◇), and 3.0 (⋆): (a) $D = 20$ mm; (b) 30 mm. Open symbols, $\langle\bar{\alpha}\rangle = 0.006$; closed symbols, 0.011. In vertical axes, the size of minor ticks is 0.03 and some example values are given.

at $-0.5 < x/D < 0.5$. This is interesting because the liquid-velocity gradient becomes steeper in the wake (Figs. 18 and 19), which would increase the shear-induced turbulence. However, the decrease of liquid-velocity fluctuation with a larger D indicates that the added contribution of shear-induced turbulence is not significant compared to the change in bubble-induced fluctuation, which is also evidenced in the decrease of Reynolds stress with a larger D (Fig. 22). The dominance of bubble-induced fluctuation in the cylinder wake is identified based on the PDF of liquid-velocity fluctuations (see Fig. 24), which is the basis of our model for bubble-induced fluctuation (see Sec. V). As shown in Fig. 7, with a larger D, the recovery of void fraction defect in the wake becomes slower, that is, there are less bubbles in the near wake region. Since the interaction of wakes behind bubbles has been considered to be the main source of bubble-induced turbulence [2,9], the lower void fraction in the wake would result in the decrease of the bubble-induced fluctuation. It is also possible that as the ratio $\langle\bar{d}_b\rangle/D$ decreases, i.e., the length scale responsible for the turbulence generation is reduced compared to the characteristic length scale of the flow, the level of turbulence is reduced. However, the size of the cylinder does not affect the turbulence at $|x/D| > 0.5$. The turbulence level in the downstream region outside of the cylinder is proportional to $\langle\bar{\alpha}\rangle^{0.4}$ [Fig. 23(a)]; however, it shows a deviation from the scaling relation at $|x/D| < 0.5$. This indicates that the disturbance caused by the existence of the circular cylinder is quite localized and the undisturbed bubbly flow maintains the upstream characteristics. In the following section, we derive a streamwise velocity fluctuation model by considering the disturbance due to the circular cylinder added to the existing fluctuating velocity in the homogeneous bubble swarm, which shows a good agreement with the measured data both in the regions away from ($|x/D| \gtrsim 0.5$) and behind ($|x/D| \lesssim 0.5$) the cylinder (see Fig. 28).

The transverse component follows the void distribution in the wake (Fig. 21). As shown, the $u'_{l,\mathrm{rms}}$ has local maximum peaks near the cylinder edge and a minimum valley behind the cylinder

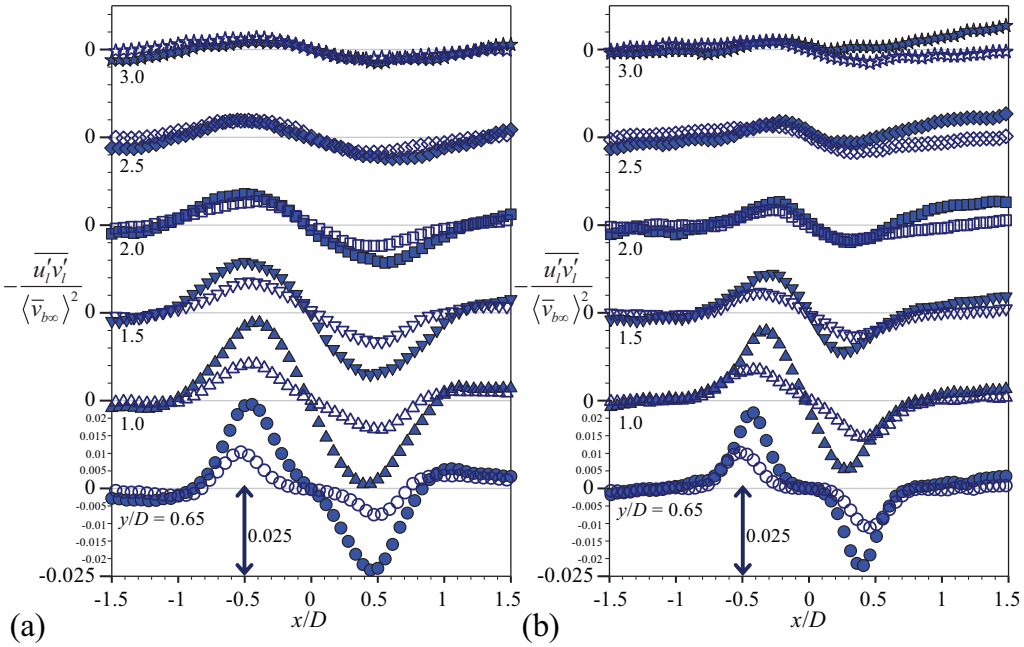

FIG. 22. Transverse distributions of the turbulent stress ($-\overline{u_l'v_l'}$) of liquid phase in the wake behind a cylinder at $y/D = 0.65$ (○), 1.0 (△), 1.5 (▽), 2.0 (□), 2.5 (◇), and 3.0 (⋆): (a) $D = 20$ mm; (b) 30 mm. Open symbols, $\langle\bar{\alpha}\rangle = 0.006$; closed symbols, 0.011. In vertical axes, the size of minor ticks is 0.005 and some example values are given.

base in the near wake ($y/D < 2.0$), according to the lateral migration of bubbles. For regime II, the two maximum peaks are in close proximity and a broad peak near $x/D \simeq 0$ is induced along the streamwise direction. In particular, the magnitude of maximum $u'_{l,\mathrm{rms}}$ becomes the largest at $y/D \simeq 1.5$ where bubbles that are separated by both sides of the cylinder converge [Figs. 7(b) and 7(e)], and decreases as the bubbles disperse. Actually, the transverse turbulence intensity profile shows the most distinct difference between the two regimes, because it is most strongly affected by the wake structure responsible for the oscillating paths of rising bubbles. The transverse turbulence

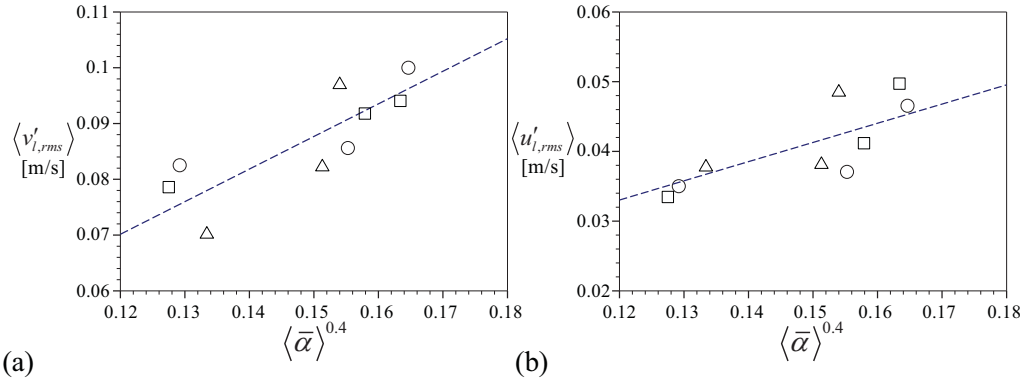

FIG. 23. Scaling relation between bubble-induced liquid velocity fluctuation and $\langle\bar{\alpha}\rangle$: (a) streamwise velocity fluctuation; (b) transverse velocity fluctuation: ○, measured at upstream; △, outside of the nearwake ($|x/D| > 0.5$) for $D = 20$ mm; □, $D = 30$ mm.

intensity outside of the cylinder ($|x/D| > 0.5$) increases from 0.12 to 0.16 as $\langle\bar{\alpha}\rangle$ increases from 0.006 to 0.011. Together with the liquid-phase velocity data for $\langle\bar{\alpha}\rangle = 0.0095$, we also find that the scaling relation of $\langle u'_{l,\mathrm{rms}}\rangle/\langle\bar{v}_{b\infty}\rangle \sim \langle\bar{\alpha}\rangle^{0.4}$ is still valid for the downstream flow at $|x/D| > 0.5$ [Fig. 23(b)]. The ratio between $v'_{l,\mathrm{rms}}$ and $u'_{l,\mathrm{rms}}$ is approximately 2 : 1, which agrees well with that measured for a laminar upward bubbly pipe flow [18,19] and bubble plume [49], in which the considered gas-phase conditions ($\langle\bar{\alpha}\rangle$ and Re) are similar to those in our study.

The turbulent stress ($-\overline{v'_l u'_l}$) has an antisymmetric profile; two peaks (with opposite signs) are located at the cylinder edge and they converge to zero along the transverse direction [Fig. 22]. In particular, the turbulent stress is very strong in the near wake region ($y/D \lesssim 1.5$) and decays quite fast at $y/D \gtrsim 2.0$ as the bubbles disperse and void distributions become uniform. The local peaks of the turbulent stress increase with as the mean void fraction increases, but decrease slightly as the cylinder size increases. In the case of $D = 20$ mm, the turbulent stress peaks tend to spread widely along the transverse direction, as the flow develops [Fig. 22(a)]; however, it is confined to quite a narrow region (along the separating shear layers) for the case of $D = 30$ mm [Fig. 22(b)]. The difference between two void fractions becomes smaller for the case of $D = 30$ mm, which is again attributed to the reduced size of the bubble wake relative to the length scale of the flow, indicating the dominant effect of bubble-induced fluctuation compared to the shear-induced turbulence.

V. MODELING OF THE BUBBLE-INDUCED FLUCTUATION

As we have shown above, even with a small void fraction, substantial liquid-flow agitation is induced and this phenomenon has been studied vigorously for its academic and industrial importance. Owing to its fluctuating nature, the bubble-induced agitation has been frequently compared to the single-phase flow turbulence and various approaches were taken to study it [18,19,50,51]. The agitation in a bubbly flow is decomposed into single-phase turbulence due to shear in the flow (without bubbles) and bubble-induced fluctuation. The interaction between these two contributions also needs to be considered [16]. The bubble-induced fluctuation is further considered as a combination of turbulent (instability of wake-induced flow) and nonturbulent (drift effect (potential flow) and mean flow) contributions [52]. In this section, we are aiming at modeling the bubble-induced fluctuation. We consider the present flow condition to be a good problem to solve, because a solid obstacle (circular cylinder) modifies (re-distribute) the bubble-induced fluctuation, as well.

In this study, we adopt the idea of a single-phase turbulence model but consider the effect of multiple-bubble induced flows together. Among the previous approaches, the eddy-diffusivity-based (ϵ_b) model [50] expresses the bubble-induced shear stress as $-\overline{u'_l v'_l} \sim \epsilon_b(\partial\bar{v}_l/\partial x)$, where $\epsilon_b = c\bar{\alpha}\langle\bar{d}_b\rangle\langle\bar{v}_b\rangle$ (c: empirical constant) is derived by assuming the mixing length (l_B) to be analogous to that of the single-phase turbulence model. The mixing length was obtained from the drift velocity in the potential flow. It is noted that the higher-order closure equations for two-phase turbulence has been also investigated for the purpose of Eulerian-Eulerian two-fluid simulations [52,53]. Their main objective was to decompose the Reynolds stress into turbulent (by wake-induced instability) and nonturbulent contributions (by an inviscid liquid drift and average wake). As shown below, the present model is quite straightforward to interpret and relevant to the breakdown into each of these contributions.

First, we analyzed the PDF of the liquid velocity fluctuations in the wake ($0.5 \leqslant y/D \leqslant 3.0$) behind a circular cylinder, to check that the bubble-induced agitation contributes dominantly while the destabilization of the mean flow is negligible in the present flow. As shown in Fig. 24, the PDFs of the streamwise and transverse velocity fluctuation (for $\langle\bar{\alpha}\rangle = 0.006, 0.0095$ and 0.011) show the typical trends of bubble-induced agitation both at $|x/D| \leqslant 0.5$ and $|x/D| > 0.5$ [2,11,13]. The streamwise velocity exhibits an asymmetric behavior (positive skewness) for all $\langle\bar{\alpha}\rangle$'s. In addition, the PDFs decay with a slight exponential tail, known as the signature of the bubble wake. The transverse velocity is symmetrically distributed. Obviously, these characteristics are

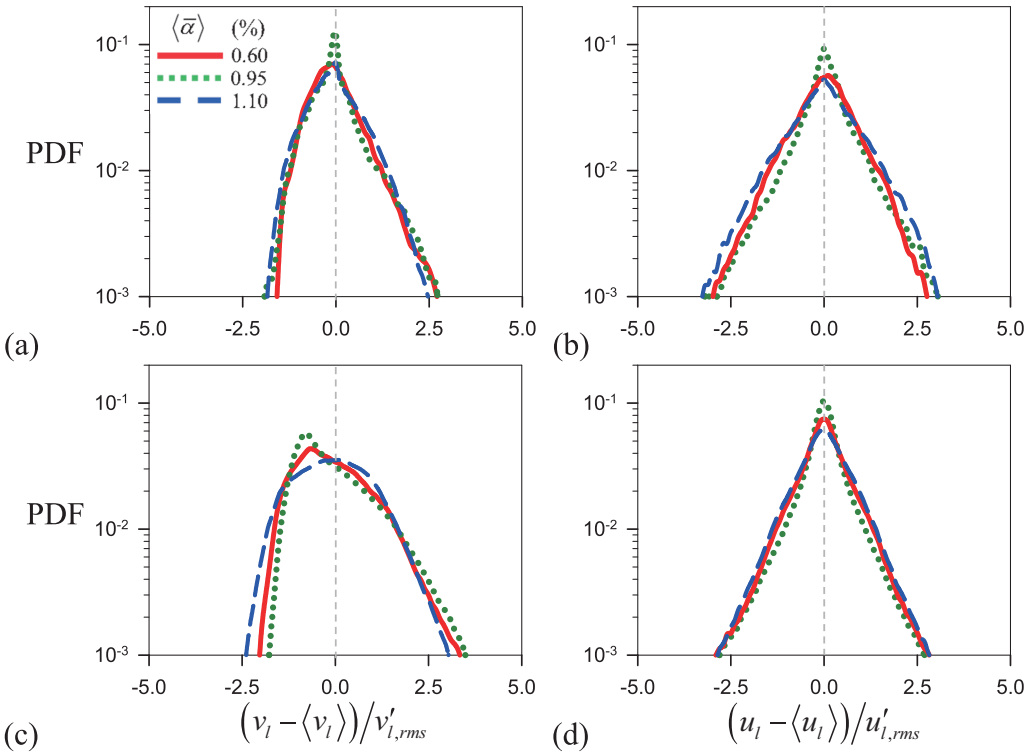

FIG. 24. Probability density function (PDF) of the liquid-phase velocity in (a), (c) streamwise and (b), (d) transverse directions, measured in the wake ($0.5 \leqslant y/D \leqslant 3.0$) behind the circular cylinder at $|x/D| \leqslant 0.5$ (a), (b) and $|x/D| > 0.5$ (c), (d).

different from the velocity fluctuation PDF resulting from the mean velocity destabilization in single-phase turbulent flows, in which a Gaussian distribution is measured for a homogeneous isotropic turbulence [11] or an asymmetric distribution with a slight negative skewness for a fully developed channel flow [54]. Thus, it is reasonable to consider the bubble-induced agitation only in the present cases. Although the global shape of the PDF inside the wake ($|x/D| \leqslant 0.5$) is similar to those outside ($|x/D| > 0.5$) and of upstream (both are mainly affected by the bubbles), it is found that the width of the transverse (streamwise) velocity fluctuation PDF becomes wider (narrower) compared to those measured outside of the wake and upstream. This indicates that the bubble-induced flows are more agitated along the transverse direction because of the presence of the cylinder.

Next, let us explain how we deal with the velocity fluctuation. Our approach to model the bubble-induced streamwise velocity fluctuation (v'_l) is to decompose the contributions from upstream flow (homogeneous bubble swarm) and the disturbance by cylinder. The first source is well established such that it is scaled to the void fraction as $v'_l \sim V_\circ \langle \bar{\alpha} \rangle^{0.4}$, where $V_\circ$ is the terminal bubble rise velocity [2,5,8,13]. If we define the additional disturbances by cylinder as $\Delta v'_l$, then we have an expression of $v'_l \sim V_\circ \langle \bar{\alpha} \rangle^{0.4} + \Delta v'_l$. As mentioned, Sato and Sekoguchi [50] assumed that the additional streamwise velocity fluctuation due to rising bubbles is proportional to the mean liquid velocity gradient and characteristic mixing length (l_B) as $\Delta v'_l \sim l_B \cdot (\partial \bar{v}_l / \partial x)$. The limitation of Sato's model is that it only considers the contribution under the inviscid flow assumption (potential flow around a two-dimensional circular cylinder). In our prior work, we suggested the implementation of the effect of the wake-induced flow from individual bubbles and showed that the predicted Reynolds stress distributions agree well with the experimental data in upward laminar

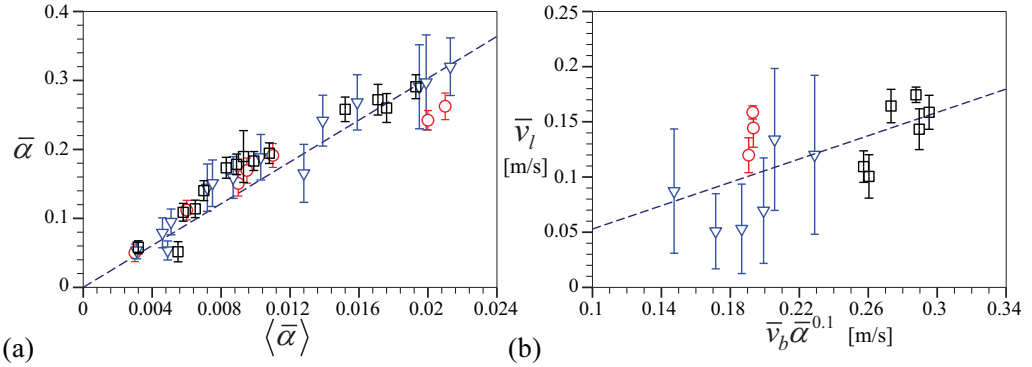

FIG. 25. (a) Linear relation between $\langle\bar{\alpha}\rangle$ and $\bar{\alpha}$; (b) scaling relation between $\bar{v}_l$ and $\bar{v}_b\bar{\alpha}^{0.1}$. ○, measured at upstream; ▽, inside the wake ($|x/D| \leqslant 0.5$, $y/D = 1.0$); □, outside the wake ($|x/D| > 0.5$).

bubbly flows [19]. However, the effect of multiple bubbles (i.e., void fraction dependency), which was not included, would need to be taken into account further. Thus, we additionally placed a second cylindrical bubble at a distance of $l_m = (\pi/6\langle\bar{\alpha}\rangle^{-1})^{1/3}\langle\bar{d}_b\rangle$ (see Fig. 27). We assumed that the bubbles (of size $\langle\bar{d}_b\rangle$) are uniformly distributed with a distance of l_m, corresponding to $\langle\bar{\alpha}\rangle$. Indeed the effect of the wake of the leading bubble on the trailing bubble still cannot be included, but the deflection (or reduction) of liquid drift due to the neighboring bubble can be formulated as a function of $\langle\bar{\alpha}\rangle$. Details of the derivation are provided in Appendix A, and the new mixing length is obtained as

$$l_B = c\langle\bar{d}_b\rangle(1 - 0.4\langle\bar{\alpha}\rangle^{2/3})f(\eta^*, \kappa). \tag{2}$$

Here, function f is expressed with two variables: η^*, the dimensionless distance from the bubble center and $\kappa = \langle\bar{d}_b\rangle/l_m$, which is understood to be a kind of blockage ratio by bubbles [see Eq. (A4)]. Thus, the function f can be absorbed into the empirical constants in the following formulation. Compared to the previous model [50], this suggests that l_B is affected by $\langle\bar{\alpha}\rangle$ such that it decreases as $\langle\bar{\alpha}\rangle$ increases.

To consider the bubble-wake effect (turbulent contribution) together, we use the scaling relation in which the streamwise mean liquid velocity ($\bar{v}_l$) by a bubble rising in quiescent water is proportional to the terminal velocity (V_o) [55,56]. As we have discussed above, the empirical relation between the mean bubble rise velocity and the void fraction has been suggested as $\bar{v}_b \sim V_o\langle\bar{\alpha}\rangle^{-0.1}$ for a homogeneous bubble swarm [2] and confirmed (Fig. 12). Considering all of these collectively, we can deduce that $\bar{v}_l \sim V_o \sim \bar{v}_b\langle\bar{\alpha}\rangle^{0.1} \sim \bar{v}_b\bar{\alpha}^{0.1}$. Because we are interested in the spatial (local) variation of turbulence statistics, we further substitute $\langle\bar{\alpha}\rangle$ with the local void fraction, $\bar{\alpha}$. This does not violate the scaling relation based on the linear correlation between $\langle\bar{\alpha}\rangle$ and $\bar{\alpha}$ [Fig. 25(a)]. We also checked whether the resultant scaling relation of $\bar{v}_l \sim \bar{v}_b\bar{\alpha}^{0.1}$ is valid for the present study. As shown in Fig. 25(b), this relation is approximately satisfied, and the largest deviation (approximately 13% on average) exists inside the wake ($|x/D| \leqslant 0.5$). Thus, we consider it is reasonable to apply this correlation to the cylinder wake. Therefore, the mean liquid shear ($\partial\bar{v}_l/\partial x$) is further derived by differentiating $\bar{v}_l \sim \bar{v}_b\bar{\alpha}^{0.1}$ with x as

$$\frac{\partial\bar{v}_l}{\partial x} \sim \bar{\alpha}^{0.1}\frac{\partial\bar{v}_b}{\partial x} + 0.1\bar{v}_b\bar{\alpha}^{-0.9}\frac{\partial\bar{\alpha}}{\partial x}. \tag{3}$$

Then, the streamwise velocity fluctuation [$v_l' \sim V_\circ\langle\bar{\alpha}\rangle^{0.4} + l_B \cdot (\partial\bar{v}_l/\partial x)$] can be expressed as

$$v_l' = c_1\bar{v}_b\bar{\alpha}^{0.1}\langle\bar{\alpha}\rangle^{0.4} + c_2\bar{d}_b(1 - 0.4\bar{\alpha}^{2/3})\left[\bar{\alpha}^{0.1}\frac{\partial\bar{v}_b}{\partial x} + 0.1\bar{v}_b\bar{\alpha}^{-0.9}\frac{\partial\bar{\alpha}}{\partial x}\right]. \tag{4}$$

Here c_1 and c_2 are empirical constants. In Eq. (4), the first term refers to the contribution from homogeneous bubble-swarm (upstream) and the second one comes from the bubbles re-distributed by cylinder. In Appendix B, we explained how the accuracy of v_l' model is checked by comparing the root-mean-square of v_l' with the measured data. As shown, the estimated $v_{l,\mathrm{rms}}'$ matches the measurement well even in the cylinder wake region ($|x/D| \lesssim 0.5$), supporting our approach to superpose the upstream and the perturbation by the cylinder.

Together with Eq. (4) for v_l', we adopt the model for the transverse liquid fluctuation (u_l') based on the drift velocity calculation, suggested by Milne-Thomson [57]. Then, we draw the Reynolds stress ($-\overline{v_l'u_l'}$) model by integrating $v_l'u_l'$ along the range around a bubble [50]. Detailed procedures appear in Appendix B.

$$-\overline{v_l'u_l'} = c_{1r}\langle \bar{d}_b\rangle\langle \bar{v}_b\rangle(1-0.4\bar{\alpha}^{2/3})\bar{\alpha}^{1.1}\frac{\partial \bar{v}_l}{\partial x} + c_{2r}(1-0.4\bar{\alpha}^{2/3})\left(\bar{d}_b\bar{v}_b\bar{\alpha}^{1.1}\frac{\partial \bar{v}_r}{\partial x} + 0.1\bar{d}_b\bar{v}_b^2\bar{\alpha}^{0.1}\frac{\partial \bar{\alpha}}{\partial x}\right). \tag{5}$$

The first term on the right-hand side is similar to the Sato's model (the contribution of the mean liquid velocity gradient but the mixing length is corrected to have $\langle\bar{\alpha}\rangle$-dependency), and the effect of the local bubble wake is expressed by the gradients of the relative bubble velocity and void fraction (the second and third terms). Previously, Hosokawa and Tomiyama [18] and Ma *et al.* [58] also suggested that additional flow variables other than the mean liquid velocity gradient are necessary to reliably predict the bubble-induced turbulence in more complex flows. This is important because the role of an individual bubble wake plays a major role in characterizing the bubble-induced turbulence, as the bubble Reynolds number and void fraction increase [9]. In Eq. (5), c_{1r} and c_{2r} are to be determined empirically.

We have compared the estimated bubble-induced Reynolds stress in the wake (Fig. 26) with the measured data. In each case, the empirical coefficients in the model were determined using the least-squares method. For all cases, the estimation using the present model is in a reasonably good agreement with the spatially varying bubble-induced turbulence in the cylinder wake; in particular, the magnitudes of local peaks and the corresponding locations are well matched. Application of the present model involves the determination of prefactors that may change depending on the flow condition and geometry; however, the range of variation seems to be more or less narrow. This is rather helpful to enhance our physical understanding on the dominant contributions from the liquid- and gas-phase statistics to the bubble-induced liquid fluctuations, especially in complex flow geometries like the present one. For example, the contributions by c_{1r} and c_{2r} are initially comparable at very near wake ($y/D \leqslant 1.0$), indicating that effects by the bubble-induced mean liquid shear ($\partial\bar{v}_l/\partial x$) and local bubble behavior ($\partial\bar{v}_r/\partial x$, $\partial\bar{\alpha}/\partial x$) are both important, because the bubble distribution is disturbed most significantly by the circular cylinder. As the flow develops, the uniform void distribution recovers and thus the values of c_2 is reduced, whereas that of c_1 becomes larger at $y/D > 1.0$.

Considering the performance of the present model, despite its simplicity because of the lower order mixing length assumption, it is possible to learn the importance of considering the contributions of the local void fraction and bubble velocity to predict the bubble-induced agitations in more complex geometries. The concept of superposing the additional flow agitation to the existing one is also supported while modeling the fluctuating velocity in bubbly flows. Since the present model accounts for the bubble-induced flow as well as the potential flow effect (increase in $\langle\bar{\alpha}\rangle$ strengthens the influence of bubble wakes), it is expected to be useful even at a higher void fraction. However, the void fraction dependencies of the bubble rise velocity ($\bar{v}_b \sim \langle\bar{\alpha}\rangle^{-0.1}$) and the liquid velocity fluctuation ($v_{l,\mathrm{rms}}' \sim \langle\bar{\alpha}\rangle^{0.4}$) on which the present model is based were validated for the void fractions up to $\langle\bar{\alpha}\rangle \simeq 0.1$ [8]. As a separate study, it is thus necessary to check (and enhance) whether the proposed model can be applied to different geometries with a higher volume void fraction under dynamic water condition (with nonzero velocity of continuous-phase flow), where a complex interaction between the wall-generated liquid shear (SIT) and the bubble-induced turbulence (BIT) is expected, resulting in different turbulence modification (e.g., enhancement or suppression).

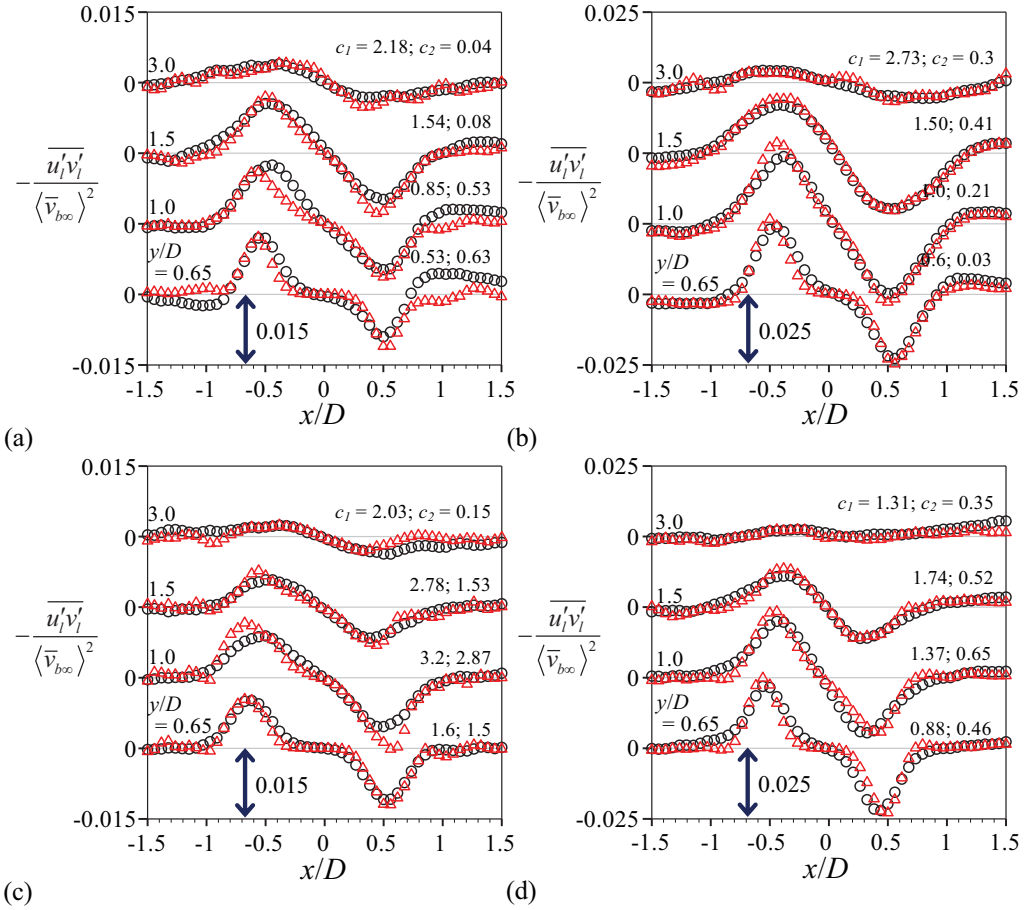

FIG. 26. Comparison between the modeled (△) and measured (○) distribution of turbulent stress behind the cylinder of (a), (b) $D = 20$ mm and (c), (d) 30 mm: (a), (c) $\langle \bar{\alpha} \rangle = 0.006$; (b), (d) 0.011. In each subfigure, the values of resultant prefactors are given.

VI. CONCLUDING REMARKS

The gas-liquid bubbly flow is a fundamental and important topic in multiphase flow problems and thus our knowledge of this complex flow is expanding quite fast. However, it is also true that most previous efforts focused on a homogenous bubble swarm in a large chamber or bubbly flows in a straight pipe (or channel), and the consideration of additional complexity in the geometry is not yet mature. From this point of view, we studied the disturbance of the bubble-swarm flow (uniform at an upstream location) as a result of the existence of a circular cylinder (larger than the bubbles), and measured both the gas and liquid phases simultaneously while varying the upstream void fraction and effective bubble size. In the considered range, the effect of the circular cylinder persists for as far as five cylinder diameters in the wake, beyond which the uniform flow statistics recover. This is quite a short distance and suggests that the vigorous momentum transfer due to interacting bubbles would be responsible for the fast dispersion of the flow. This is supported by the fact that recovery of the uniform flow is delayed and the bubble-induced turbulence is reduced as the size of the cylinder increases, i.e., the added contribution of shear-induced turbulence is not significant and the length scale of bubble-induced agitation is reduced compared to the characteristic length scale of the flow.

For the gas phase, the void distribution in the wake region was classified into two regimes. When the upstream void fraction is relatively small, the bubbles show higher concentrations along the separating shear-layers of the cylinder (regime I). As the void fraction increases, bubbles migrate rapidly toward the center of the wake where they produce a broad peak there (regime II). By calculating the interfacial forces acting on bubbles, it was found that the lateral migration of bubbles toward the center of the cylinder as a result of pressure gradient and shear-induced lift forces is prevented by the repelling force due to the drag in regime I. However, in regime II, the shear-induced lift force becomes dominant and thus the bubbles migrate toward the central region of the wake center.

As the only source of liquid flow is rising bubbles, the liquid flow would clearly be dominantly affected by the void distribution; e.g., it is locally accelerated in areas in which there are more bubbles and the bubble-induced liquid fluctuation scales with the void fraction. This modification in the flow is the key idea of developing bubble-induced Reynolds stress model. That is, the contributions of bubble wakes, represented by the transverse gradients of the void fraction and bubble velocity, are included in addition to that of the liquid velocity gradient. The present bubble-induced turbulence model successfully estimated the spatially varying turbulent stress in the cylinder wake for both regimes. Considering the range of the volume void fraction ($\leqslant 2.1\%$), however, it would be necessary to check whether the proposed model would remain valid for a higher void fraction and to overcome the inevitable inclusion of prefactors. We are currently applying the present model to data available in the literature to verify whether the model can estimate the turbulent stress in other situations and to seek the universal ranges of the prefactors, as well.

Although we placed one additional solid obstacle in the bubbly flow, most practical multiphase flows would be more complex than the present configuration. However, we would like to emphasize that it is possible to measure and understand the variation of both gas and liquid phases, and furthermore physically model the turbulence variation in the flow. We expect the present results to be useful for understanding and controlling the gas-liquid flows around more complex solid geometries.

ACKNOWLEDGMENTS

This work was supported by Grants No. 2016R1C1B2012775, No. 2017M2A8A4018482, and No. 2020R1A2 C22014510 through the National Research Foundation of Korea (NRF), funded by the Korean government (MSIT) via SNU-IAMD, and also by the Institute of Engineering Research and Entrepreneurship at Seoul National University.

APPENDIX A: DERIVATION OF MIXING LENGTH

We obtain the mixing length from the flow displacement (drift) in a side-by-side cylinder arrangement. In Fig. 27, the two points $P_1\ (-\infty, y_1)$ and $P_2\ (0, y_2)$ are located on the same streamline ($\psi = \psi_1$) in the vicinity of a rising bubble (radius $a = \langle \bar{d}_b \rangle/2$). The liquid drifts at these points P_1 and P_2 are affected by the main bubble and deflected upward ($\Delta y_{\text{up}} > 0$); however, they are also affected by the neighboring bubble at a distance of l_m, being pushed downward simultaneously ($\Delta y_{\text{down}} < 0$). Therefore, the net displacement, $\Delta y_{\text{up}} - \Delta y_{\text{down}}$, determines the effective liquid drift. The streamline can be analytically expressed by the linear superposition of the stream function for uniform flow and two doublets, as follows:

$$\psi = U_\infty \Big[y - a^2 \Big(\frac{y}{x^2 + y^2} + \frac{y - l_m}{x^2 + (y - l_m)^2} \Big) \Big], \tag{A1}$$

where U_∞ is the bubble rise velocity. It is clear that the mixing length (l_B) in this flow is related to the displacement ($y_2 - y_1$) over which point P_2 is drifted by the existence of both bubbles, and

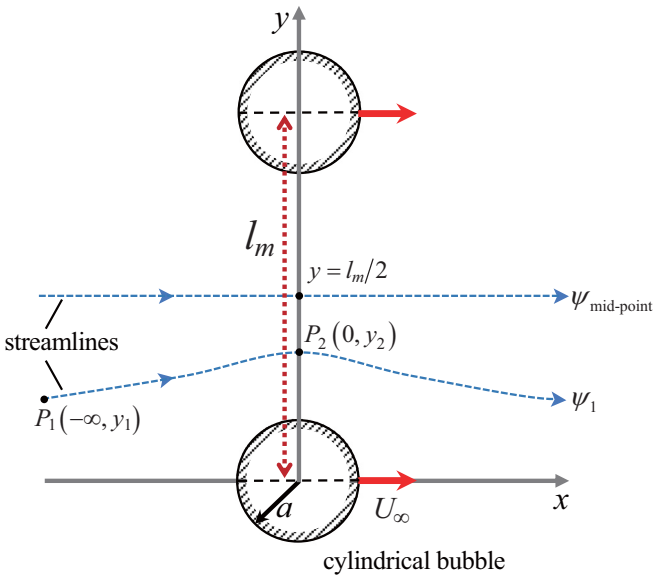

FIG. 27. Schematic diagram of side-by-side cylindrical bubbles in a potential flow. The distance between bubbles is l_m, and two points P_1 and P_2 are located on the same streamline ($\psi = \psi_1$). U_∞ is the rise velocity of bubbles.

$y_2 - y_1$ can be calculated as follows:

$$y_2 - y_1 = -a^2\left(\frac{1}{l_m - y_2} - \frac{1}{y_2}\right). \tag{A2}$$

Assuming $|y_2/l_m| < 1.0$, which is reasonable for the considered low void fraction condition, we apply a Taylor expansion to the first term on the right-hand side of Eq. (A2). Then it is expressed as $(l_m^2 + a^2)y_2^2 - l_m(l_m y_1 - a^2)y_2 - a^2 l_m^2 = 0$. By solving this second-order equation, the mixing length ($l_B \simeq y_2 - y_1$) is obtained as follows:

$$l_B \simeq \frac{\langle \bar{d}_b \rangle}{2(1 + (\kappa/2)^2)} \cdot f(\eta^*, \kappa), \tag{A3}$$

where

$$f(\eta^*, \kappa) = \sqrt{(\eta^* - \kappa/4)^2 + \kappa^2/4 + 1} - (1 + \kappa^2/2)\eta^* - \kappa/4. \tag{A4}$$

Here, $\eta^* = y_1/(2a)$ and $\kappa = \langle \bar{d}_b \rangle / l_m$. It is noted that the mixing length is related to the bubble size and the spacing between bubbles. In the nondimensional function, $f(\eta^*, \kappa)$, the variable κ would be considered as a constant, because we assumed the uniform distribution of bubbles. Equation (A3) is subject to a Taylor series expansion by assuming $\kappa < 1.0$ (this assumption is valid for a low to moderate void fraction):

$$l_B = c\langle \bar{d}_b \rangle (1 - 0.4\langle \bar{\alpha} \rangle^{2/3}) f(\eta^*, \kappa). \tag{A5}$$

APPENDIX B: FORMULATION OF BUBBLE-INDUCED AGITATION

1. Root-mean-square of streamwise velocity fluctuation

First, we estimate the root-mean-square of streamwise velocity fluctuation ($v'_{l,\text{rms}}$) based on our model for v'_l [Eq. (4)]. The variations in the streamwise liquid fluctuation at a distance η^* from the

centroid of a bubble (Fig. 27) is expressed as Eq. (B1):

$$v'_{l,\mathrm{rms}}|_{\eta^*} = c_1 \bar{v}_b \bar{\alpha}^{0.1} \langle\bar{\alpha}\rangle^{0.4} + c_2 \bar{d}_b (1 - 0.4\bar{\alpha}^{2/3}) f(\eta^*, \kappa) \left[\bar{\alpha}^{0.1} \frac{\partial \bar{v}_b}{\partial x} + 0.1 \bar{v}_b \bar{\alpha}^{-0.9} \frac{\partial \bar{\alpha}}{\partial x} \right]. \tag{B1}$$

Assuming that the liquid displacements caused by individual bubbles are independent each other, the contributions of each bubble can be superposed (integrated) along the region of $-1/(2\kappa) \leqslant \eta^* \leqslant 1/(2\kappa)$, and the result is given as follows:

$$\begin{aligned} v'_{l,\mathrm{rms}} = & \int_{-1/2\kappa}^{1/2\kappa} c_1 d\eta^* \cdot \bar{v}_b \bar{\alpha}^{0.1} \langle\bar{\alpha}\rangle^{0.4} + \int_{-1/2\kappa}^{1/2\kappa} c_2 f(\eta^*, \kappa) d\eta^* \cdot \bar{d}_b (1 - 0.4\bar{\alpha}^{2/3}) \\ & \times \left[\bar{\alpha}^{0.1} \frac{\partial \bar{v}_b}{\partial x} + 0.1 \bar{v}_b \bar{\alpha}^{-0.9} \frac{\partial \bar{\alpha}}{\partial x} \right]. \end{aligned} \tag{B2}$$

Since the integrals can be treated as prefactors, the r.m.s. of streamwise velocity fluctuation can be shortened as follows:

$$v'_{l,\mathrm{rms}} = c_1 \bar{v}_b \bar{\alpha}^{0.1} \langle\bar{\alpha}\rangle^{0.4} + c_2 \bar{d}_b (1 - 0.4\bar{\alpha}^{2/3}) \left[\bar{\alpha}^{0.1} \frac{\partial \bar{v}_b}{\partial x} + 0.1 \bar{v}_b \bar{\alpha}^{-0.9} \frac{\partial \bar{\alpha}}{\partial x} \right]. \tag{B3}$$

We have compared the estimated $v'_{l,\mathrm{rms}}$ with the measured data in Fig. 28. The empirical prefactors determined using the least-square method are shown together. In all cases, the present model matches the spatially varying fluctuation. The prefactors are in the range of $6 < c_1 < 7$ and $0 < c_2 < 2$. c_2 initially is around 2.0 at $y/D < 1.5$ but decreases slowly; the wakes of local bubbles in the cylinder wake are initially influential but it decays gradually. Eventually, c_1 becomes larger than c_2 in downstream, indicating that the flow turbulence only reflects that from homogeneous bubble swarm.

2. Reynolds stress

To calculate the Reynolds stress, together with our model for v'_l, we adopt the transverse velocity fluctuation (u'_l) model from the drift velocity suggested by Milne-Thomson [57]:

$$u'_l|_{\eta^*} \sim \begin{cases} \langle\bar{v}_b\rangle & (|\eta^*| < 1.0), \\ \langle\bar{v}_b\rangle/\eta^{*2} & (|\eta^*| \geqslant 1.0). \end{cases} \tag{B4}$$

Same as the streamwise velocity fluctuation, the contributions of each bubble can be superposed (integrated) along the region of $-1/2\kappa \leqslant \eta^* \leqslant 1/2\kappa$:

$$-\overline{v'_l u'_l} = \int_{-1/2\kappa}^{1/2\kappa} u'_l|_{\eta^*} v'_l|_{\eta^*} \cdot \bar{\alpha}(\eta^*) d\eta^*. \tag{B5}$$

Substituting Eqs. (4) and (B4) into Eq. (B5), the following Eq. (B6) is obtained:

$$\begin{aligned} & -\overline{v'_l u'_l} \\ & \sim \int_{-1/2\kappa}^{-1} \left[\bar{\alpha} V_\circ \langle\bar{\alpha}\rangle^{0.4} \frac{\langle\bar{v}_b\rangle}{\eta^{*2}} + (1 - 0.4\langle\bar{\alpha}\rangle^{2/3}) \langle\bar{d}_b\rangle \langle\bar{v}_b\rangle \bar{\alpha} \left(\bar{\alpha}^{0.1} \frac{\partial \bar{v}_b}{\partial x} + 0.1 \bar{v}_b \bar{\alpha}^{-0.9} \frac{\partial \bar{\alpha}}{\partial x} \right) \frac{f(\eta^*, \kappa)}{\eta^{*2}} \right] d\eta^* \\ & + \int_{-1}^{1} \left[\bar{\alpha} V_\circ \langle\bar{\alpha}\rangle^{0.4} \langle\bar{v}_b\rangle + (1 - 0.4\langle\bar{\alpha}\rangle^{2/3}) \langle\bar{d}_b\rangle \langle\bar{v}_b\rangle \bar{\alpha} \left(\bar{\alpha}^{0.1} \frac{\partial \bar{v}_b}{\partial x} + 0.1 \bar{v}_b \bar{\alpha}^{-0.9} \frac{\partial \bar{\alpha}}{\partial x} \right) f(\eta^*, \kappa) \right] d\eta^* \\ & + \int_{1}^{1/2\kappa} \left[\bar{\alpha} V_\circ \langle\bar{\alpha}\rangle^{0.4} \frac{\langle\bar{v}_b\rangle}{\eta^{*2}} + (1 - 0.4\langle\bar{\alpha}\rangle^{2/3}) \langle\bar{d}_b\rangle \langle\bar{v}_b\rangle \bar{\alpha} \left(\bar{\alpha}^{0.1} \frac{\partial \bar{v}_b}{\partial x} + 0.1 \bar{v}_b \bar{\alpha}^{-0.9} \frac{\partial \bar{\alpha}}{\partial x} \right) \frac{f(\eta^*, \kappa)}{\eta^{*2}} \right] d\eta^*. \end{aligned} \tag{B6}$$

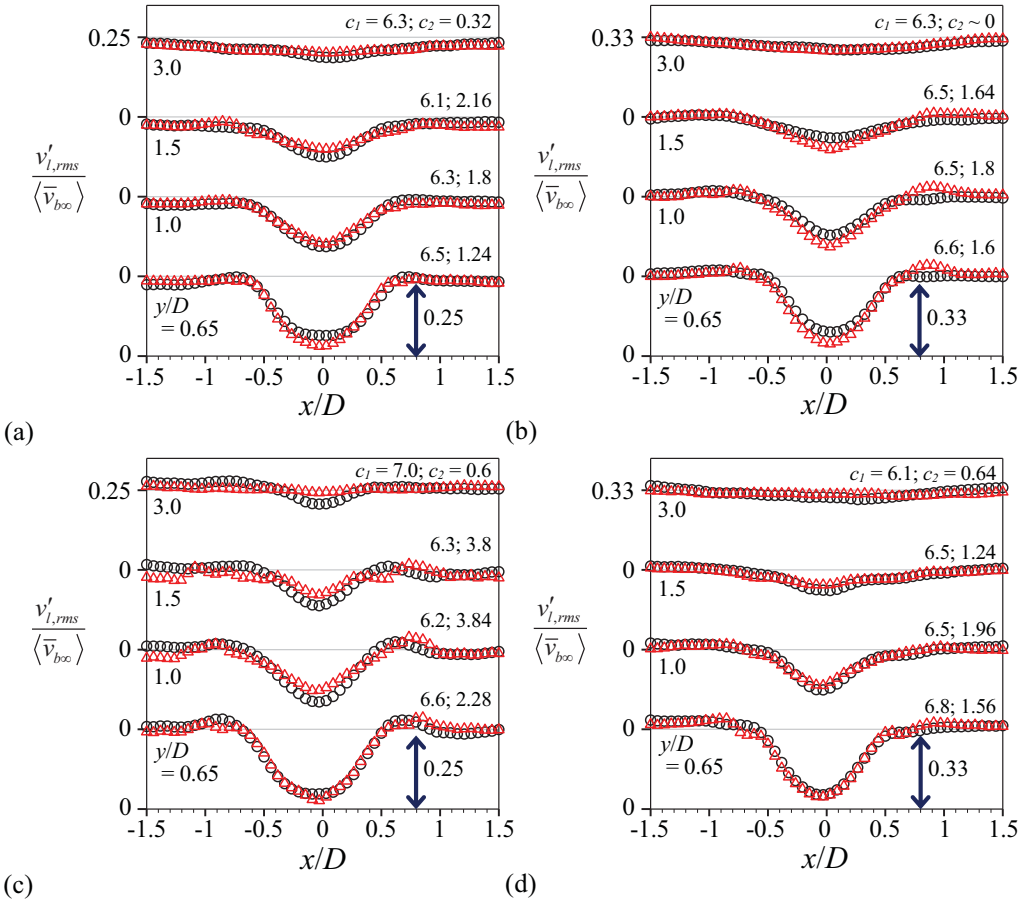

FIG. 28. Comparison between the modeled (△) and measured (○) distribution of $v'_{l,\mathrm{rms}}$ behind the cylinder of (a), (b) $D = 20$ mm and (c), (d) 30 mm: (a), (c) $\langle \bar{\alpha} \rangle = 0.006$; (b), (d) 0.011. In each subfigure, the values of resultant prefactors are given.

After arranging this equation as

$$-\overline{v'_l u'_l} \sim \bar{\alpha} V_\circ \langle \bar{\alpha} \rangle^{0.4} \langle \bar{v}_b \rangle \left[\int_{-1/2\kappa}^{1/2\kappa} \frac{1}{\eta^{*2}} d\eta^* + 4 \right] + (1 - 0.4\langle \bar{\alpha} \rangle^{2/3}) \langle \bar{d}_b \rangle \langle \bar{v}_b \rangle \bar{\alpha} \left(\bar{\alpha}^{0.1} \frac{\partial \bar{v}_b}{\partial x} + 0.1 \bar{v}_b \bar{\alpha}^{-0.9} \frac{\partial \bar{\alpha}}{\partial x} \right) \times \left[\int_{-1/2\kappa}^{-1} \frac{f(\eta^*, \kappa)}{\eta^{*2}} d\eta^* + \int_{-1}^{1} f(\eta^*, \kappa) d\eta^* + \int_{1}^{1/2\kappa} \frac{f(\eta^*, \kappa)}{\eta^{*2}} d\eta^* \right], \tag{B7}$$

the integral terms in parentheses can be treated as an empirical constant and this equation can further expanded with the definition of relative velocity, $\bar{v}_r = \bar{v}_b - \bar{v}_l$:

$$-\overline{v'_l u'_l} \sim \bar{\alpha} \langle \bar{v}_b \rangle V_\circ \langle \bar{\alpha} \rangle^{0.4} + (1 - 0.4\alpha^{2/3}) \langle \bar{d}_b \rangle \langle \bar{v}_b \rangle \left(\bar{\alpha}^{1.1} \frac{\partial \bar{v}_l}{\partial x} + \bar{\alpha}^{1.1} \frac{\partial \bar{v}_r}{\partial x} + 0.1 \bar{v}_b \bar{\alpha}^{0.1} \frac{\partial \bar{\alpha}}{\partial x} \right). \tag{B8}$$

Similar to the relation between $\langle \bar{\alpha} \rangle$ and $\bar{\alpha}$, we may find the relations of $\langle \bar{d}_b \rangle \sim \bar{d}_b$ and $\langle \bar{v}_b \rangle \sim \bar{v}_b$ are satisfied in the present cases (Fig. 29). Thus, we replace $\langle \bar{d}_b \rangle$ and $\langle \bar{v}_b \rangle$ with $c' \bar{d}_b$ and $c'' \bar{v}_b$,

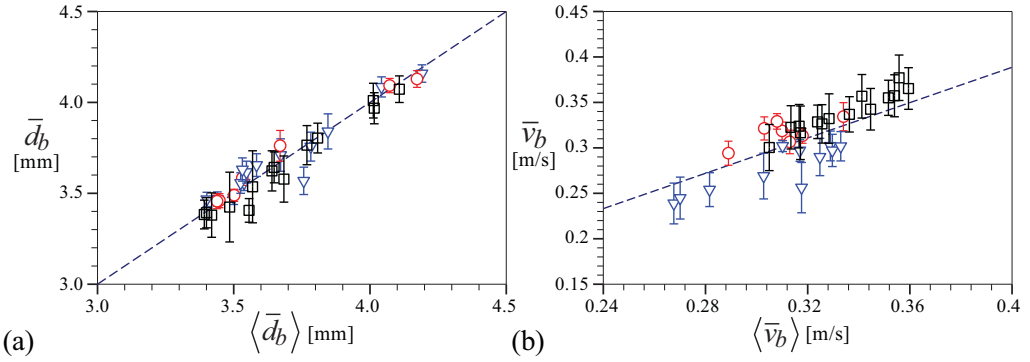

FIG. 29. Linear relation between the local statistics with global values of (a) bubble size; (b) bubble rise velocity; ○, measured at upstream; ▽, in the wake ($|x/D| \leqslant 0.5$, $y/D = 1$); □, outside the wake ($|x/D| > 0.5$).

respectively. This is to consider the local effect of bubbles and thus it is applied to the second ($\partial \bar{v}_r/\partial x$) and third ($\partial \bar{\alpha}/\partial x$) terms. Applying this relation, the Reynolds stress is expressed as follows:

$$-\overline{v_l' u_l'} = c_{0r}\bar{\alpha}\langle \bar{v}_b \rangle V_\circ \langle \bar{\alpha} \rangle^{0.4} + c_{1r}\langle \bar{d}_b \rangle \langle \bar{v}_b \rangle (1 - 0.4\bar{\alpha}^{2/3})\bar{\alpha}^{1.1}\frac{\partial \bar{v}_l}{\partial x} + c_{2r}(1 - 0.4\bar{\alpha}^{2/3})\left(\bar{d}_b \bar{v}_b \bar{\alpha}^{1.1}\frac{\partial \bar{v}_r}{\partial x} + 0.1\bar{d}_b \bar{v}_b^2 \bar{\alpha}^{0.1}\frac{\partial \bar{\alpha}}{\partial x}\right). \tag{B9}$$

When Eq. (B9) is applied, we find that the coefficient c_{0r} becomes always zero. Indeed the first term only is symmetric (against $x/D = 0$) and all others are asymmetric. Thus, it is reasonable to ignore the first term, and the Reynolds stress model is finalized as

$$-\overline{v_l' u_l'} = c_{1r}\langle \bar{d}_b \rangle \langle \bar{v}_b \rangle (1 - 0.4\bar{\alpha}^{2/3})\bar{\alpha}^{1.1}\frac{\partial \bar{v}_l}{\partial x} + c_{2r}(1 - 0.4\bar{\alpha}^{2/3})\left(\bar{d}_b \bar{v}_b \bar{\alpha}^{1.1}\frac{\partial \bar{v}_r}{\partial x} + 0.1\bar{d}_b \bar{v}_b^2 \bar{\alpha}^{0.1}\frac{\partial \bar{\alpha}}{\partial x}\right). \tag{B10}$$

[1] S. Balachandar and J. K. Eaton, Turbulent dispersed multiphase flow, Annu. Rev. Fluid Mech. **42**, 111 (2010).

[2] F. Risso, Agitation, mixing, and transfers induced by bubbles, Annu. Rev. Fluid Mech. **50**, 25 (2018).

[3] M. Lance and J. Bataille, Turbulence in the liquid phase of a uniform bubbly air-water flow, J. Fluid Mech. **222**, 95 (1991).

[4] R. Zenit, D. L. Koch, and A. S. Sangani, Measurements of the average properties of a suspension of bubbles rising in a vertical channel, J. Fluid Mech. **429**, 307 (2001).

[5] F. Risso and K. Ellingsen, Velocity fluctuations in a homogeneous dilute dispersion of high-Reynolds-number rising bubbles, J. Fluid Mech. **453**, 395 (2002).

[6] J. Rensen, S. Luther, and D. Lohse, The effect of bubbles on developed turbulence, J. Fluid Mech. **538**, 153 (2005).

[7] V. Roig and A. Larue de Tournemine, Measurement of interstitial velocity of homogeneous bubbly flows at low to moderate void fraction, J. Fluid Mech. **572**, 87 (2007).

[8] G. Riboux, F. Risso, and D. Legendre, Experimental characterization of the agitation generated by bubbles rising at high Reynolds number, J. Fluid Mech. **643**, 509 (2010).

[9] G. Riboux, D. Legendre, and F. Risso, A model of bubble-induced turbulence based on large-scale wake interactions, J. Fluid Mech. **719**, 362 (2013).

[10] E. Alméras, F. Risso, V. Roig, S. Cazin, C. Plais, and F. Augier, Mixing by bubble-induced turbulence, J. Fluid Mech. **776**, 458 (2015).
[11] E. Alméras, V. Mathai, D. Lohse, and C. Sun, Experimental investigation of the turbulence induced by a bubble swarm rising within incident turbulence, J. Fluid Mech. **825**, 1091 (2017).
[12] D. Colombet, D. Legendre, F. Risso, A. Cockx, and P. Guiraud, Dynamics and mass transfer of rising bubbles in a homogenous swarm at large gas volume fraction, J. Fluid Mech. **763**, 254 (2015).
[13] F. Risso, Physical interpretation of probability density functions of bubble-induced agitation, J. Fluid Mech. **809**, 240 (2016).
[14] J. Martínez-Mercado, C. A. Palacios-Morales, and R. Zenit, Measurement of pseudoturbulence intensity in monodispersed bubbly liquids for $10 < \mathrm{Re} < 500$, Phys. Fluids **19**, 103302 (2007).
[15] V. N. Prakash, J. Martínez-Mercado, L. van Wijngaarden, E. Mancilla, Y. Tagawa, D. Lohse, and C. Sun, Energy spectra in turbulent bubbly flows, J. Fluid Mech. **791**, 174 (2016).
[16] A. du Cluzeau, G. Bois, and A. Toutant, Analysis and modeling of Reynolds stresses in turbulent bubbly up-flows from direct numerical simulations, J. Fluid Mech. **866**, 132 (2019).
[17] C. C. Lai and S. A. Socolofsky, The turbulent kinetic energy budget in a bubble column, J. Fluid Mech. **865**, 993 (2019).
[18] S. Hosokawa and A. Tomiyama, Bubble-induced pseudo turbulence in laminar pipe flows, Int. J. Heat Fluid Flow **40**, 97 (2013).
[19] M. Kim, J. H. Lee, and H. Park, Study of bubble-induced turbulence in upward laminar bubbly pipe flows measured with a two-phase particle image velocimetry, Exp. Fluids **57**, 55 (2016).
[20] A. Inoue, Y. Kozawa, M. Yokosawa, and A. Aoki, Studies on two-phase cross flow. Part I: Flow characteristics around a cylinder, Int. J. Multiphase Flow **12**, 149 (1986).
[21] B. V. R. Vittal and W. Tabakoff, Two-phase flow around a two-dimensional cylinder, AIAA J. **25**, 648 (1987).
[22] M. P. Païdoussis, A review of flow-induced vibrations in reactors and reactor components, Nucl. Eng. Des. **74**, 31 (1983).
[23] M. Yokosawa, Y. Kozawa, A. Inoue, and S. Aoki, Studies on two-phase cross flow. Part II: Transition Reynolds number and drag coefficient, Int. J. Multiphase Flow **12**, 169 (1986).
[24] Y. Joo and V. K. Dhir, An experimental study of drag on a single tube and on a tube in an array under two-phase cross flow, Int. J. Multiphase Flow **20**, 1009 (1994).
[25] M. J. Pettigrew and C. E. Taylor, Two-phase flow-induced vibration: An overview (survey paper), J. Pressure Vessel Technol. **116**, 233 (1994).
[26] K. Sugiyama, S. Takagi, and Y. Matsumoto, Three-dimensional numerical analysis of bubbly flow around a circular cylinder, JSME Int. J., Ser. B **44**, 319 (2001).
[27] R. Lindken and W. Merzkirch, A novel PIV technique for measurements in multiphase flows and its application to two-phase bubbly flows, Exp. Fluids **33**, 814 (2002).
[28] D. Bröder and M. Sommerfeld, Planar shadow image velocimetry for the analysis of the hydrodynamics in bubbly flows, Meas. Sci. Technol. **18**, 2513 (2007).
[29] G. Mougin and J. Magnaudet, Wake-induced forces and torques on a zigzagging/spiralling bubble, J. Fluid Mech. **567**, 185 (2006).
[30] P. Ern, F. Risso, D. Fabre, and J. Magnaudet, Wake-induced oscillatory paths of bodies freely rising or falling in fluids, Annu. Rev. Fluid Mech. **44**, 97 (2012).
[31] J. Lee and H. Park, Wake structures behind an oscillating bubble rising close to a vertical wall, Int. J. Multiphase Flow **91**, 225 (2017).
[32] Y. Kim and H. Park, Upward bubbly flows in a square pipe with a sudden expansion: Bubble dynamics and reattachment length, Int. J. Multiphase Flow **118**, 254 (2019).
[33] G. S. West and C. J. Apelt, The effects of tunnel blockage and aspect ratio on the mean flow past a circular cylinder with Reynolds numbers between 10^4 and 10^5, J. Fluid Mech. **114**, 361 (1982).
[34] N. J. Lawson, M. Rudman, A. Guerra, and J. L. Liow, Experimental and numerical comparisons of the break-up of a large bubble, Exp. Fluids **26**, 524 (1999).
[35] N. Kim, H. Kim, and H. Park, An experimental study on the effects of rough hydrophobic surfaces on the flow around a circular cylinder, Phys. Fluids **27**, 085113 (2015).

[36] J. Sauvola and M. Pietikäinen, Adaptive document image binarization, Pattern Recognit. **33**, 225 (2000).
[37] M. J. Sathe, I. H. Thaker, T. E. Strand, and J. B. Joshi, Advanced PIV-PLX-SOL-PLXLIF and shadowgraphy system to visualize flow structure in two phase bubbly flows, Chem. Eng. Sci. **65**, 2431 (2010).
[38] R. C. Gonzalez, R. E. Woods, and S. L. Eddins, *Digital Image Processing using MATLAB* (McGraw-Hill Education, New York, NY, 2011).
[39] N. Otsu, A threshold selection method from gray-level histograms, IEEE Trans. Syst. Man. Cybern. **9**, 62 (1979).
[40] Y. M. Lau, N. G. Deen, and J. A. M. Kuipers, Development of an image measurement technique for size distribution in dense bubbly flows, Chem. Eng. Sci. **94**, 20 (2013).
[41] M. Pang and J. Wei, Experimental investigation on the turbulence channel flow laden with small bubbles by PIV, Chem. Eng. Sci. **94**, 302 (2013).
[42] R. Clift, J. R. Grace, and M. E. Weber, *Bubbles, Drops, and Particles* (Academic Press, San Diego, CA, 1978).
[43] D. Drew and R. T. Lahey, Jr., The virtual mass and lift forces on a sphere in a rotating and straining flow, Int. J. Multiphase Flow **13**, 113 (1987).
[44] M. E. Shawkat, C. Y. Ching, and M. Shoukri, Bubble and liquid turbulence characteristics of bubbly flow in a large diameter vertical pipe, Int. J. Multiphase Flow **34**, 767 (2008).
[45] A. du Cluzeau, G. Bois, A. Toutant, and J.-M. Martinez, On bubble forces in turbulent channel flows from direct numerical simulations, J. Fluid Mech. **882**, A27 (2020).
[46] M. Ishii and N. Zuber, Drag coefficient and relative velocity in bubbly, droplet or particulate flows, AIChE J. **25**, 843 (1979).
[47] T. Hibiki and M. Ishii, Lift force in bubbly flow systems, Chem. Eng. Sci. **62**, 6457 (2007).
[48] R. Adoua, D. Legendre, and J. Magnaudet, Reversal of the lift force on an oblate bubble in a weakly viscous linear shear flow, J. Fluid Mech. **628**, 23 (2009).
[49] M. Simiano, D. Lakehal, M. Lance, and G. Yadigaroglu, Turbulent transport mechanisms in oscillating bubble plumes, J. Fluid Mech. **633**, 191 (2009).
[50] Y. Sato and K. Sekoguchi, Liquid velocity distribution in two-phase bubble flow, Int. J. Multiphase Flow **2**, 79 (1975).
[51] M. Colombo and M. Fairweather, Multiphase turbulence in bubbly flows: RANS simulations, Int. J. Multiphase Flow **77**, 222 (2015).
[52] J. Chahed, V. Roid, and L. Masbernat, Eulerian-Eulerian two-fluid model for turbulent gas-liquid bubbly flows, Int. J. Multiphase Flow **29**, 23 (2003).
[53] G. Bellakhel, J. Chahed, and L. Masbernat, Analysis of the turbulence statistics and anisotropy in homogeneous shear bubbly flow using a turbulent viscosity model, J. Turbul. **5**, N36 (2004).
[54] B. Castaing, Y. Gagne, and E. J. Hopfinger, Velocity probability density functions of high Reynolds number turbulence, Physica D **46**, 177 (1990).
[55] G. K. Batchelor, *An Introduction to Fluid Dynamics* (Cambridge University Press, Cambridge, UK, 1967).
[56] K. Ellingsen and F. Risso, On the rise of an ellipsoidal bubble in water: Oscillatory paths and liquid-induced velocity, J. Fluid Mech. **440**, 235 (2001).
[57] L. M. Milne-Thomson, *Theoretical Hydrodynamics* (Macmillan, New York, NY, 1968).
[58] M. Ma, J. Lu, and G. Tryggvason, Using statistical learning to close two-fluid multiphase flow equations for a simple bubbly system, Phys. Fluids **27**, 092101 (2015).